A Linear Paul Trap for Ytterbium Ions

A thesis submitted in partial fulfillment
of the requirements for the degree of

Master of Science

by

Phillip Wieburg

on 30th of April 2014

ILP
INSTITUT FÜR LASERPHYSIK

Supervised by

Prof. Dr. Henning Moritz

Phillip Wieburg:

A Linear Paul Trap for Ytterbium Ions

Master Thesis
Universität Hamburg

Zusammenfassung

Ionenfallenexperimente ermöglichten vor etwa 30 Jahren erstmals die hochpräzise Untersuchung der quantenmechanischen Eigenschaften einzelner gefangener Atome. Seitdem haben solche Experimente große Fortschritte im Bereich der Spektroskopie sowie der Quanteninformationsverarbeitung geliefert. In der Quanteninformationsverarbeitung bieten gefangene Ionen bis heute die besten physikalischen Realisierungen von Quantenbits und Quantengattern. Hier profitieren sie vor allem von der guten Isolierbarkeit der Ionen von der Umgebung und ihrer starken Wechselwirkung untereinander. Gleichzeitig offenbarte sich ein breites Spektrum an weiteren Anwendungsmöglichkeiten, beispielsweise zur Untersuchung fundamental quantenmechanischer Probleme oder der Wechselwirkung von Ionen mit ultrakalten Quantengasen.

Im Rahmen dieser Masterarbeit wurde ein experimenteller Aufbau zur Durchführung von Experimenten mit gefangenen Ytterbiumionen entworfen und realisiert. Als Ionenfalle dient dabei eine lineare Paulfalle. Der Aufbau ist dafür optimiert, ein möglichst breites Spektrum an späteren Anwendungen zu ermöglichen. Dazu musste das Experiment insbesondere hinsichtlich der Fallenfrequenzen, des optischen Zugangs sowie der Güte des Vakuums optimiert werden. Außerdem waren eventuell erfolgende Erweiterungen des Experiments zu berücksichtigen. Zu dem experimentellen Aufbau zählen neben der Ionenfalle selbst ein Ultrahochvakuumsystem, ein System zur Erzeugung der Radiofrequenz, drei Lasersysteme sowie abbildende Optik zur Detektion der Ionen. Da eines der notwendigen Lasersysteme nicht rechtzeitig fertig gestellt werden konnte, wurde der Aufbau im Rahmen dieser Masterarbeit noch nicht erfolgreich zum Fangen von Ionen benutzt.

Nach einer Zusammenfassung der Historie sowie der Anwendungen von Ionenfallen stellt diese Masterarbeit zunächst die physikalischen Grundlagen der Dynamik von Ionen in Paulfallen dar, um anschließend den Konstruktionsprozess, den Aufbau und die Inbetriebnahme der notwendigen Systeme zu beschreiben.

Abstract

About 30 years ago, experiments with trapped ions enabled physicists for the first time, to investigate the quantum behavior of single trapped atoms. Since this time, such experiments led to significant progress in the fields of spectroscopy and quantum information processing. Today, trapped ions provide the best physical realizations of quantum bits and quantum gates. This is mostly due to the fact that ions can be isolated very well from the environment and interact strongly between each over. Besides, several other applications of trapped ions where developed. For example, trapped ions are used for probing most fundamental quantum mechanical systems such as coupled harmonic oscillators or for investigating interactions between ions and ultracold quantum gases.

In this master thesis a setup for experiments with trapped ytterbium ions was designed and realized. As ion trap design, a linear Paul trap was used. During the design process, the setup was optimized for making a broad spectrum of different types of experiments possible. This included optimization with respect to trapping frequencies, optical access and the vacuum system. Additionally, possible extensions had to be taken into account. The setup consists of a linear Paul trap, an ultra high vacuum system, a system used for providing the radio frequency, three laser systems and an optical imaging system used for ion detection. Due to the fact that one of the laser systems could not be finished on time, the setup could not be used for ion trapping attempts within the time of this master thesis.

This master thesis starts with an overview of the historic development of ion trapping and its applications as well as the fundamentals of Paul traps. Afterwards, design, assembly and commissioning of the necessary technical systems is described in detail.

Contents

Chapter 1

Introduction

Physics seeks to understand nature on a fundamental level. Such an understanding based on a small set of first principles can most easily be obtained by investigating nature's properties in systems with a small number of degrees of freedom making - at least within some well-argued approximations - the formulation of a theory and the comparison of the theory's predictions with experimental results possible.

An ideal system for testing and extending the fundamental physical principles consists of one atom, or a small number of atoms. Millennia after ancient natural philosophers formulated the idea of quantized matter, ion trapping experiments enabled mankind for the first time to perform experiments with single trapped atoms.

This chapter gives an overview of the historic development, typical applications and challenges of ion trapping.

1.1   History of Ion Trapping

In 1989, Wolfgang Paul was awarded with the Nobel Prize in physics for the development of the radio frequency ion trap. Honoring his work, radio frequency ion traps are named after him. In the same year, Hans G. Dehmelt was awarded the price for his achievements in trapping ions using only time-independent electric and magnetic fields. Such ion traps are usually known as Penning traps. Due to the influence of the magnetic trapping field on the internal quantum states of the ion, they are mostly used if magnetic properties such as Zeeman splittings or magnetic moments are to be measured. In the following, only radio frequency ion traps are considered.

The field of ion trapping developed from molecular beam physics and mass spectrometry. A first ion trap was realized by W. Paul in 1954, as reported in his Nobel lecture [51] - a good starting point for studying ion traps. There, he starts by explaining the principle of quadrupole mass filters, which pro-

duce a two-dimensional confinement, before introducing ion traps. Indeed, the linear Paul traps that are typically used nowadays are almost identical to the two-dimensional quadrupole mass filters W. Paul patented in 1953. These mass filters consist of four rods producing an oscillating electric quadrupole field being passed longitudinally by an ion beam. The quadrupole field has, if parameters are chosen correctly, a focusing effect on the ions. Physically and mathematically, this is very similar to the principle of strong focusing found in accelerator physics.[1] As the stability of the trajectory of the ions passing the filter depends on the mass, a mass spectrum of the ion beam can be obtained by varying the quadrupole field appropriately, for example by adding a time-independent quadrupole field, which is always defocusing in one direction. In order to use such a configuration as an ion trap, one simply has to add two additional electrodes put on static positive potential. Interestingly, W. Paul did not use this electrode configuration producing a two-dimensional quadrupole field, but another configuration which produces a three-dimensional quadrupole field. It consists of a ring electrode, and two hyperbolic cap electrodes. A sketch of such a trap is shown in figure 2.4. Radio frequency is applied to the ring, while a DC field can be applied to the caps. This field configuration is sometimes said to produce a spherical trap, in the sense that no direction is distinguishable. However, for this type of Paul trap, the trapping frequencies are not necessarily identical. Nonetheless, these traps will sometimes be called spherical in the following. A better term for spherical ion traps would be "point-like" as the micromotion vanishes only in a single point for these traps. Mathematically, spherical and linear Paul traps are almost equivalent. In retrospect, it is quite surprising that the idea of using a modified mass filter for trapping ions was only published in 1989 in reference [52]. This paper also contains calculations proving the linear ion trap superior to the spherical ion trap due to higher ion capacity. In principle, a spherical trap can store a high number of ions as well, but most of them would have large micromotion and therefore large Doppler shifts.

Linear and spherical ion traps work with mesoscopic particles as well, such as dust or pollen. In the early days of ion trapping, experiments with aluminum particles have been performed, to obtain a better understanding of the particle orbits. The main difference between ion traps for atomic ions and mesoscopic ions is that the frequency of the oscillating quadrupole is far smaller for the latter, leading to much larger amplitudes of micromotion. A good example for such a mesoscopic ion trap is the one shown in figure 1.1.

Until linear Paul traps were first employed in the year 1990, some ground-breaking experimental achievements have been made using spherical Paul traps. In 1979 the group around P.E. Toschek succeeded in trapping, cooling and

---

[1]Details on similarities between trapped ions and ions accelerated in an alternating gradient synchrotron will be given in 2.2. These similarities have been exploited for obtaining a better understanding of beam dynamics by doing experiments with ion traps.
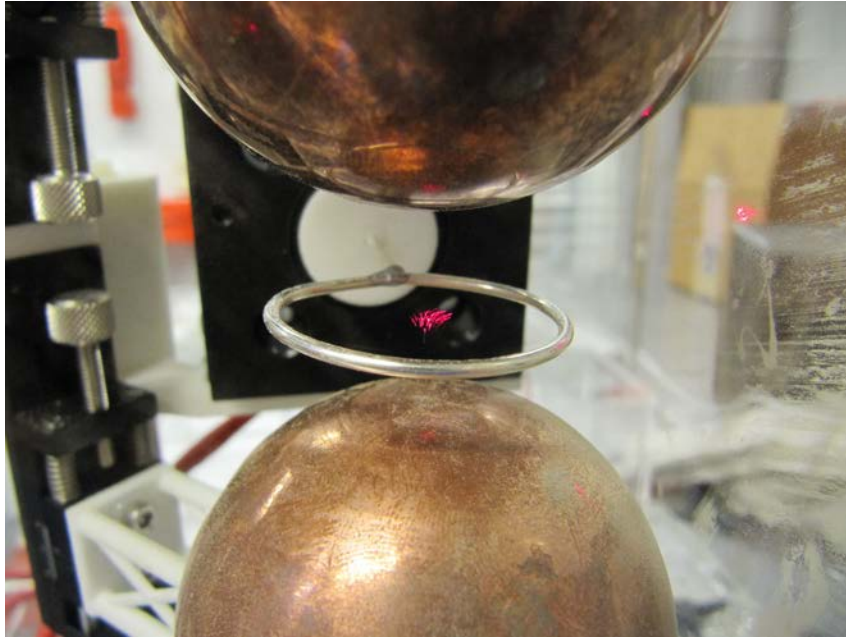
Figure 1.1: Spherical ion trap for dust particles, built by the author for demonstrative purposes. It comprises of two copper hollow spheres as cap electrodes and a silver plated copper wire as ring electrode. The cap electrodes have a diameter of 60 mm. The trap is operated using line voltage transformed to about 10 kV. As dust particles, pollen from the flower "club moss" is used. When taking this photo, the ionized pollen was illuminated with a laser pointer. Due to the large amplitude micromotion with a frequency of 50 Hz, the ions look like short strings.

imaging a single barium ion [45]. For the first time, it was possible to do experiments with single atoms. This directly led to the first observation of quantum jumps in 1986, also by the group of Toschek, reported in reference [56]. Observing quantum jumps was simply done by measuring the fluorescence of the ion illuminated with a resonant laser. When the ion spontaneously jumps into a "dark" state, no fluorescence is measured, until it suddenly jumps back. The observation of quantum jumps is only possible with a small number of ions. It has to be pointed out that the trapping of single neutral atoms is far more difficult than trapping single ions.

Considering electrode structure, the evolution of ion traps did not stop with the invention of linear Paul traps. Today, most experiments using linear traps have blade like radio frequency electrodes and small distances from the ion to the electrode surfaces of e.g. 0.5 mm, as this leads to high trapping frequencies and thereby facilitates ground state cooling. Additionally, some experiments, e.g. the one described in reference [20], make use of segmented radio frequency electrodes instead of using end-caps for longitudinal confinement. Another ongoing development is the miniaturization of ion traps down to electrode

distances of some microns. These ion traps can be built lithographically on a semiconductor chip, which might be especially useful for increasing the number of qubits in quantum computers, meaning increasing the numbers of quantum bits a quantum computer uses for its calculations. An example of such traps, in this case for cadmium ions, is given in reference [60]. A disadvantage of these chip traps is that the coherence time of quantum states prepared in the ions is comparably short, due to the close distances to surfaces. "Errors" induced by interactions between the surfaces and the ion call for sophisticated quantum error correction techniques. Details on some fundamental aspects mentioned in this paragraph can be found in subsection 1.2.2.

An interesting aspect of the history of ion trapping is the evolution of cooling mechanisms. In the early days of ion trapping, no laser cooling techniques were available. Instead, the ions were cooled by scattering with a small amount of room temperature buffer gas inside the vacuum chamber. A good example of this technique is given in reference [57], where a reduction of the ion temperature by a factor of 3 is reported by exposing the trapped barium ions to helium with a pressure of 5×10^{-6} mbar. Even now that laser cooling techniques are very well understood and building appropriate laser systems does not pose severe technological problems, buffer gases are sometimes used when new ion trap setups are put into operation. The presence of background gas reduces trapping time but facilitates first trapping attempts. Optical cooling of low density gases has been proposed simultaneously by D.J. Wineland and H. Dehmelt as well as T.W. Hänsch and A.L. Schawlow [25] in 1975. First demonstrations of the technique were published in 1978 by W. Neuhauser, M. Hohenstatt, P. Toschek and H. Dehmelt [45] and practically at the same time by D.J. Wineland, R.E. Drullinger and F.W. Walls [66]. Of course, both experiments were performed with ions. Doppler cooling generally works by illuminating atoms with narrow linewidth laser light that is red detuned with respect to an atomic transition. In the reference frame of the thermally moving atom, the light is observed to be blue detuned by the Doppler effect if the atom is moving towards the laser. Accordingly, a certain speed can tune the laser into resonance with the atom. In this case, the atom absorbs a photon and momentum is transferred to the atom, reducing its velocity. After the atom is excited, it emits a spontaneous photon, thereby converting motional energy into energy stored in the lightfield. This process happens repeatedly and cools the atoms down to the Doppler temperature. At this temperature, the width of the Boltzmann velocity distribution of the atoms has the same order of magnitude as the natural linewidth of the atomic transition used for cooling. With the natural linewidth Γ of the atomic transition, the so called "Doppler temperature", meaning the lowest temperature reachable using Doppler cooling is given by

$$T_D = \frac{\hbar \Gamma}{2 k_B} \tag{1.1}$$

Up to this point, the atoms where considered to be freely moving. In ion traps, the ions are strongly confined, rendering the physical situation different, as the quantization of motional states has to be taken into account. The quantization leads to the occurrence of sidebands in the absorption spectrum of the ions. These sidebands have been explained by R.H. Dicke in 1953 long before corresponding experiments were feasible, compare reference [17]. Now, the absorption-emission cycle described above has to change the motional energy of the atoms by exactly one quantum of harmonic oscillator energy $\hbar\omega$. An easily readable explanation of Doppler cooling for strongly confined ions has been given by W. Neuhauser in reference [46]. Detailed calculations for this physical situation as well as more sophisticated cooling techniques necessary for ground state cooling can be found in reference [21]. Luckily, the Doppler temperature for the confined case turns out to be the same as for the case of free particles. In typical ion trapping experiments, the Doppler temperature corresponds to occupation numbers of the harmonic oscillator of about 20, making further cooling necessary for most applications.

In experiments using ions with disadvantageous level structure efficient optical cooling is difficult. Besides, some experiments do not allow the presence of cooling laser radiation. One possible alternative to obtain cold ions is to use sympathetic cooling. This cooling technique works by bringing the ions into contact with atoms of another species, either neutral or ionized, that can be laser cooled more easily. For example, Wineland used laser cooled beryllium ions for sympathetically cooling mercury ions in 1986, see reference [33]. Alternatively, as reported in reference [70], it is possible to cool ions by bringing them into contact with an ultra cold quantum gas.

A very different cooling technique is the so called feedback cooling, where the ion's motional state is monitored using laser fluorescence and from this signal a feedback is generated that is applied to the trap electrodes. In reference [11], this technique is reported to be capable of cooling ions to temperatures below the Doppler limit.

1.2 Applications

This section gives an overview of interesting experiments performed with trapped ions, to open a perspective for future experiments.

1.2.1 Fundamental Quantum Mechanics

A single cold atom, trapped in a harmonic potential is a tool to probe the correctness of our knowledge about the nature of quantized harmonic oscillators. Of course, this system is of special interest to every physicist, as it is one of the few exactly solvable quantum systems and serves as a model in almost any

field of physics. Another system of great interest is the quantum mechanical two level system. Both these physical system are realized in a single, cold, electrodynamically trapped ion. Obviously, this system is modeled by the Jaynes-Cummings model, if an appropriate laser field is present for mediating the interaction between mechanical oscillator and internal ion two level system. The Jaynes-Cummings model is otherwise known from the field of cavity quantum dynamics. General testing of the Jaynes-Cummings model as well as the preparation and detections of non-classical occupation number states for the oscillator - thermal states with low mean occupation number, Fock states, coherent states and squeezed states - have been reported in references [13] and [39].

A system that is more complicated than the simple harmonic oscillator are coupled harmonic oscillators. Due to their strong Coulomb interaction, trapped ions are ideal for doing experiments with coupled harmonic oscillators in the quantum regime. The group around D.J. Wineland prepared two ions in a double well configuration, where the ions are about $40\,\mu m$ apart. The frequencies of the wells can be tuned separately. They observed periodic energy transfer between the oscillators, if the trapping frequencies of the wells are tuned into resonance, see reference [10]. It is quite obvious that extending such experiments to more than two ions and maybe to other geometric arrangements of the ions could reveal exciting physics.

1.2.2   Quantum Computing

The field of quantum computing aims at using quantum mechanical systems to build a novel kind of computer that is capable of solving certain computational problems faster than classical computers. A very prominent example of a quantum algorithm is Quantum Fourier Transformation. It can be used for rapid integer factorization of arbitrarily large numbers and is therefore a key to breaking even the strongest types of encryption known today. Many physical systems can be used for building quantum computers. Here, the fundamentals of quantum computing are shortly summarized and criterions for a good quantum computer derived. Finally, it is argued why trapped ions constitute a very promising physical realization of a quantum computer.

In quantum computers, the information is stored in coherent superpositions of the states of two-level systems. The quantum state of such a bit, called qubit, is generally written as

$$|\Psi\rangle = \alpha\,|0\rangle + \beta\,|1\rangle$$

where α and β are complex numbers with $|\alpha|^2 + |\beta|^2 = 1$. Here, the first difference between classical and quantum computation becomes evident: Quantum bits store an infinite amount of information, as the coefficients α and β can have infinitely many decimal spaces. Of course, when reading out a qubit the

wave function collapses upon measurement. The principle of a bit being in a certain state with a certain probability is called superposition. It is not known in classical computation and represents the first powerful tool for building quantum algorithms.

The second such powerful tool can be discovered when studying possible states of quantum systems comprising of multiple qubits, say two. In such systems entangled states such as the "Bell state"

$$\frac{|00\rangle + |11\rangle}{\sqrt{2}}$$

exist, where the state of the first qubit is determined when measuring the state of the second qubit. This behavior, exclusively present in quantum systems, is known as entanglement.

The third difference is that quantum gates describing operations on quantum bits are unitary operations. As a consequence, quantum gates are reversible, whereas classical gates are not. According to the standard reference for quantum computation written by M.A. Nielsen and I.L. Chuang [47] a quantum computer has to fulfill the following requirements:

- Qubits have to store the information robustly. The values of the coefficients α and β should only change if a gate operates on the qubit.

- The quantum computer has to be able to apply a universal family of unitary gates to the qubits. A set of gates forms a universal family, if every other gate can be represented by a composition of these gates.

- The initial state of the qubits has to be known very precisely.

- Finally, the quantum computer has to be able to read the state of the quantum bits.

If trapped ions are used for quantum computing, one way of defining quantum bits is to use a combination of two long living hyperfine states and motional states. Operations on quantum bits are performed by applying resonant or off-resonant laser light: Laser radiation resonant with the transition between the qubits drives Rabi-Oscillations between $|0\rangle \leftrightarrow |1\rangle$, meaning that the amplitudes of α and β oscillate periodically. Off-resonant light does not change these amplitudes, but the relative phase between the two states. As modern laser optics enables us to apply laser radiation with very well defined wavelength as well as high spatial and time resolution, optical gates can be performed with high fidelity. Multi-qubit quantum gates can be realized by addressing shared phonon states. Initialization of the qubits is achieved by cooling the ions to the motional ground state and optical pumping into the desired atomic ground state. Readout of qubits is done by illuminating the ions with resonant light

and observing fluorescence light. Ion traps benefit from the fact that stored ions can be very well isolated from the environment, hence reducing decoherence and the necessity of using quantum error control protocols. Limited scalability, meaning the increase of number of qubits, has been demonstrated: In 2011 the group around R. Blatt created an entangled state with 14 stored ions [44]. The main task of new quantum computing experiments is to increase this number. It might be achieved using novel trap geometries, facilitating for example the transports of qubits between registers. Additionally, progress is most likely to be made by using new kinds of quantum algorithms, such as the one proposed by A. Sørensen and K. Mølmer in references [59] and [42]. Here a quantum logic gate is described, where the dependence of time evolution on vibrational quantum numbers is eliminated by destructive interference of transition paths. Hence, these quantum logic gates do not require cooling the ions to the motional ground state.

Ytterbium has been successfully used for quantum information processing, as for example reported in references [3], [50] and [38]. Quantum computing with trapped ytterbium ions benefits from

- the low number of required laser wavelengths and their accessibility with diode lasers. Only two lasers are necessary for laser cooling and fluorescence imaging. One additional laser is required for photoionization.

- the possibility to load each one of the several isotopes occurring in natural ytterbium selectively into the trap.

- the occurrence of two hyperfine states in $^{171}\text{Yb}^+$ serving as a long lived qubit.

Until now the most promising results in quantum computation have been obtained using ion trap quantum computers. Nonetheless, alternatives exist and might one day lead to commercial applications, whereas trapped ions most likely will remain confined to the laboratory. These alternatives include

- Optical quantum computers, where polarization states or the location between two cavity modes of single photons serve as qubits. An advantage of these systems is that single qubit gates are easily realized by passing photons through waveplates or beamsplitters. On the other hand, mediating interactions between photons is difficult as this requires nonlinear media, or the interaction with single atoms trapped inside optical cavities. Fundamentals on optical quantum computers have been reviewed in reference [48].

- Artificial ("Cooper-pair box") atoms located in a microwave cavity. A very significant feature of such a setup is that the spectrum of resonances of the artificial atoms can be changed easily by varying external

parameters, such as electric and magnetic field. Thus, the coupling between artificial atoms, serving as qubits, and the light field, serving as bus, can be switched on and off. Details on this type of experiment can be found in reference [64].

1.2.3 Spectroscopy

The ability to perform experiments with single cold trapped atoms made it possible to analyze absorption and emission spectra with a previously unknown degree of precision. This is due to the line widening caused by the Doppler effect of the moving atom is dramatically reduced. The first order Doppler broadening is essentially eliminated in the Lamb-Dicke limit[2], compare reference [67]. The uncertainty in linewidth remaining when the atom has been cooled to the motional ground state is caused by the second order Doppler effect. Information on how to estimate the shift caused by second order Doppler effect can be found in reference [67]. It is connected with the motional energy remaining in the system after cooling. For the case of radio frequency trapped ions, this energy is increased by an amount caused by the micromotion. According to reference [67], this energy is on the same order of magnitude as the energy of the secular motion. Of course, experimenting with single atoms inside an ultra-high vacuum also eliminates pressure induced shifts as well as collective effects.

An example of how spectroscopy is performed on a narrow linewidth transition can be found in reference [54]. There, the transition $^2S_{1/2}$-$^2D_{5/2}$ of $^{171}Yb^+$ is analyzed.

---

[2]In the Lamb-Dicke limit a particle is confined so strongly that the motional state cannot be changed by the recoil energy of a photon.

Chapter 2

Trapping of Ions

This chapter summarizes the most important facts about the equation of motion of an ion located in the oscillating quadrupole field configuration produced by a Paul trap. Understanding the equation of motion is helpful for choosing experiment parameters appropriately and making predictions about the dynamics of the ions. Furthermore, effects caused by experimental imperfections are discussed. As ion traps are analogous to particle accelerators in many aspects, a deeper understanding of the dynamics in ion traps might be obtained from observations in accelerator physics and vice versa. That is why this chapter concludes with explaining this analogy and some consequences.

2.1 Dynamics of Ions in Quadrupole Traps

2.1.1 Earnshaw's Theorem

According to Earnshaw's theorem a minimum in the electric potential does not exist in a volume without electric charges and with a time-independent electric field. This follows from Maxwell's equations. As a consequence, trapping electrically charged particles with a time-independent electric field is impossible. Avoiding the general mathematical proof for this assertion, let us consider a harmonic electric potential. A particle trapped in a harmonic potential is one of the most favorable physical systems because its dynamics are simple and very well understood even in the quantum mechanical regime. Thus, the following deduction is fully satisfying. If one considers a three dimensional electric potential

$$\Phi = \alpha x^2 + \beta y^2 + \gamma z^2$$

which leads to an electric field

$$\vec{E} = -\nabla\Phi = -2 \begin{pmatrix} \alpha x \\ \beta y \\ \gamma z \end{pmatrix}$$

one of the Maxwell equations for the case without charges states

$$\nabla \cdot \vec{E} = -2 \left(\alpha + \beta + \gamma \right) = 0$$

Thus, one of the three field components has to realize a repulsive potential at any time.

2.1.2 Linear Paul Trap

An electrode geometry which produces harmonic electric potentials is a linear Paul trap. Historically, it developed from the Paul mass filter. It consists of four rod shaped electrodes and two so called end-caps, as shown in figure 2.1. An oscillating voltage is applied to the rod shaped electrodes producing an
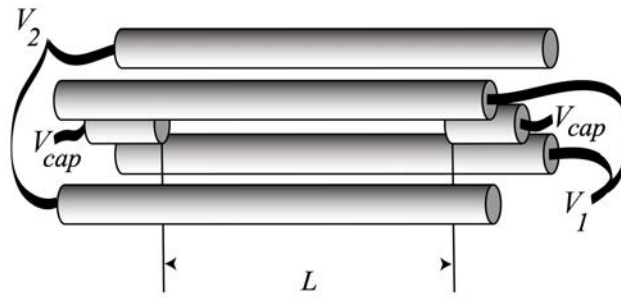
Figure 2.1: Schematic drawing of a linear Paul trap, taken from [24]. Two phases of radio frequency are applied to the rods, while a positive voltage is applied to the end-caps.

oscillating quadrupole field for radial confinement. The voltage applied to the end-caps is constant and ensures axial confinement.
In the following, the radial directions are called x and y, while the axial direction is called z. The quadrupole electrodes produce a potential

$$\Phi_{RF} \left(\vec{r}, t \right) = V_{RF} \frac{x^2 - y^2}{2r_0^2} \cos \left(\Omega t \right) \tag{2.1}$$

In a mechanical analogue this potential corresponds to a saddle shaped surface, on which a ball can be "trapped" in the center, by an adequate rotation of the surface. This is depicted in figure 2.2. The axially confining end-cap voltage leads to a potential containing radially deconfining terms:

$$\Phi_{EC} \left(\vec{r} \right) = \frac{V_{cap}}{L^2} \left(2z^2 - x^2 - y^2 \right) \tag{2.2}$$
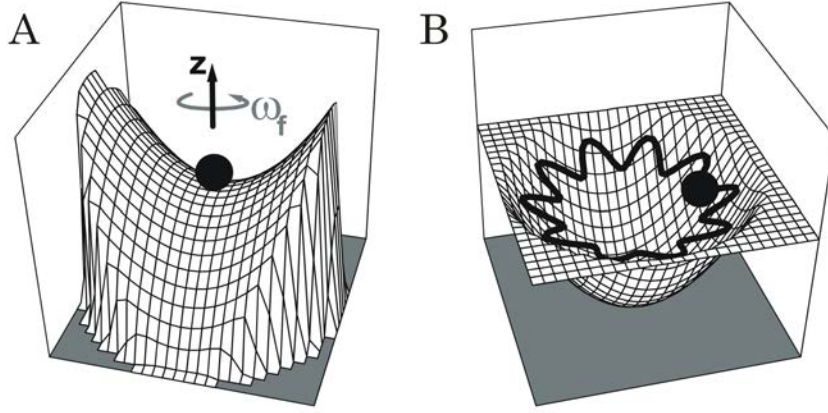
Figure 2.2: A ball on a rotating saddle surface. A mechanical analogue for Paul traps that even works in practice. In A, the ball is shown in the saddle point of the rotating potential. This potential is focusing in one direction and defocusing in the other. In B, the resulting pseudopotential as well as the trajectory of the ball is shown. As explained below, the trajectory consists of a low amplitude, rapidly oscillating component, the micromotion, and a so called secular motion. Taken from [41].

2.1.3   Equations of Motion

From the electric potential

$$\Phi\left(\vec{r},t\right) = \Phi_{RF}\left(\vec{r},t\right) + \Phi_{EC}\left(\vec{r}\right)$$

one easily obtains the equations of motion for a positively charged ion

$$\frac{d^2x}{d\tau^2} + \left(b - 2q\cos\left(2\tau\right)\right)x \quad = \quad 0 \tag{2.3}$$

$$\frac{d^2y}{d\tau^2} + \left(b + 2q\cos\left(2\tau\right)\right)y \quad = \quad 0 \tag{2.4}$$

$$\frac{d^2z}{d\tau^2} \quad +2bz = \quad 0 \tag{2.5}$$

where

$$\begin{aligned}
\tau &= \frac{1}{2}\Omega t \\
b &= \frac{e\alpha V_{cap}}{mL^2\Omega^2} \\
q &= \frac{2eV_{RF}}{mr_0^2\Omega^2}
\end{aligned} \tag{2.6}$$

Ω denotes the angular frequency of the radio frequency, V_{RF} is the amplitude of the radio frequency, e is the elementary charge, m is the mass of the ion,

and r_0 is the spacing between two quadrupole electrodes of equal phase. α is a dimensionless parameter which accounts for experimental deviations from a pure quadrupole field.[1] The equations for the radial directions are Mathieu equations, a special type of Hill equation. Axially it is just a harmonic oscillator. The exact mathematical solution to the radial equations of motion is complicated but can easily be understood as the harmonic oscillation of a mean position $\vec{r_m}$ and an oscillatory deviation $\delta\vec{r}$ from this mean position,

$$\vec{r}(t) = \vec{r_m}(t) + \delta\vec{r}(t)$$

The deviation $\delta\vec{r}$ is called micromotion. It has the same frequency as the driving field. Its existence is necessary for the trapping of particles, but one seeks to minimize the amplitude of micromotion because it adds unwanted spectroscopic features. Understanding micromotion is essential for knowing how an ion trap works. For deepening our understanding of how the existence of micromotion leads to ion trapping, let us simplify the problem by considering only one dimension and to have the sinusoidally oscillating potential replaced with a potential which discretely changes between harmonic focusing and defocusing.[2] The situation is visualized in figure 2.3. At time t_0, an ion is far away from the trap minimum, the potential is attractive. Hence, a strong electric force accelerates the ion towards the trap center. One half oscillation period later, the potential is repulsive. The ion is accelerated away from the trap center, but the force is weaker than the focusing force was, due to the particle being nearer to the trap center. Another half oscillation period later the potential is attractive again, the position slightly changed compared with the initial state. This displacement is due to the secular motion.

The existence of points where the micromotion vanishes is the best way to classify different geometries of ion traps. Historically, the first ion traps where formed by a ring and two hyperbolic caps, see figure 2.4. In this configuration, the only point where the micromotion vanishes is the center of the trap. As a consequence, it is impossible to minimize the micromotion for more than a single ion. For linear Paul traps, the micromotion vanishes on a line, enabling us to minimize the micromotion for a large number of ions in an ion crystal.

Experimentally, electric offset fields, e.g. produced by static charges on isolating materials near the ion trap, shift the mean ion position into regions of larger RF amplitude and larger micromotion, as visualized in 2.5. Therefore it is necessary to compensate for such unwanted fields by applying DC electric voltages to the RF electrodes or to additional compensation electrodes.

---

[1]In order to produce a perfect quadrupole field, one would have to choose infinitely large, hyperbolically shaped electrodes for the radio frequency.

[2]One should note that this time development of the potential is basically the same typically found in the frame of rest of a particle traveling along a FODO structure. FODO is the term typically used in accelerator physics for a magnetic beam optic comprising of alternating focusing and defocusing quadrupole magnets.
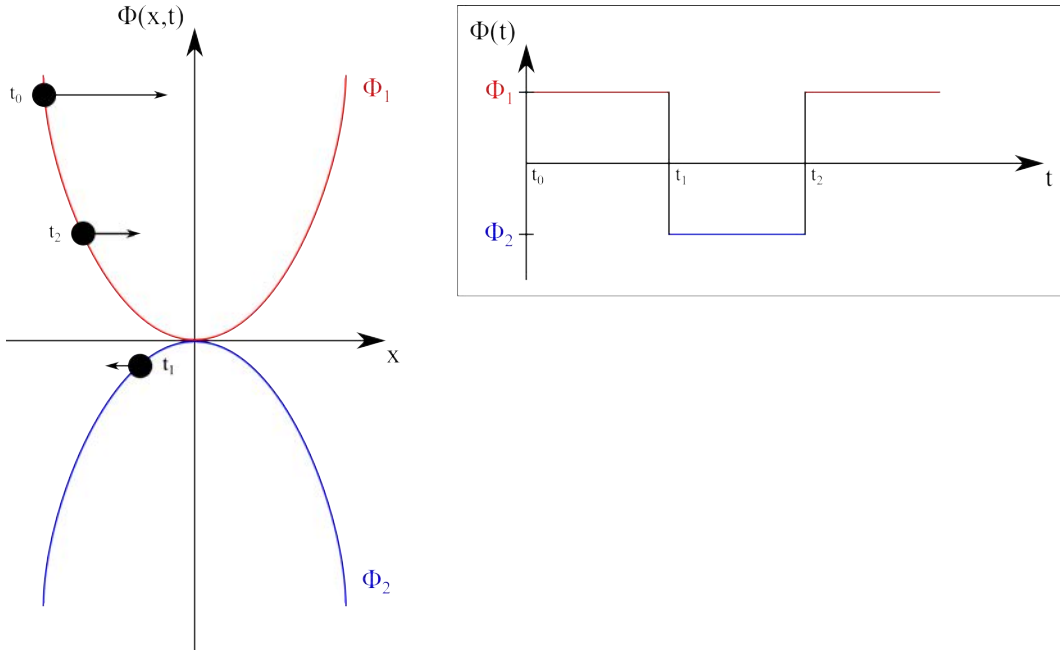
Figure 2.3: A particle trapped in a one dimensional oscillating harmonic potential, for visualizing the principle of RF ion trapping. The amplitude of micromotion is strongly exaggerated. Another noteworthy aspect of this scheme is the frequency of the potential switching being much larger than the secular motion of the particle in the effective harmonic potential. Thus, the particle being "lower" in the oscillator after one micromotion period should not be confused with a dissipative effect. At the times shown, the particle is not necessarily at rest - kinetic energy is not visualized in this scheme. A detailed explanation is given in the text.

This is done by detecting the micromotion spectroscopically and minimizing it. Methods for detecting micromotion have been described and experimental results reported in [6].

For the ideal linear Paul trap, the question, whether the motion is - for given parameters b and q as defined above - stable, can be decided using the stability diagram shown in figure 2.6. It contains the lowest regions of stability for the linear Paul trap as well as for the mass filter. Experimentally, only stability region A is relevant. For low b and q, the stability regions for ion trap and ion mass filter are identical, besides the fact that for the ion trap, the parameter b is restricted to negative values. A positive b corresponds to negatively charged end-cap electrodes, which would obviously lead to a deconfining potential. If the magnitude of b is chosen too large, the radially deconfining effect of the electric field produced by the end-caps makes the radial motion unstable. For q being large, the amplitude of micromotion becomes too large leading to ion loss. This is visualized, again in a physically simplified picture, in figure 2.7.
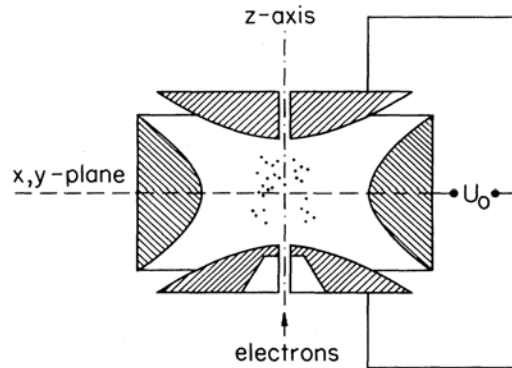
Figure 2.4: Schematic view of the historic Paul trap, taken from [51]. It is a section view of a cylinder symmetric geometry. Radio frequency is applied to a hyperbolically shaped ring and two hyperbolic caps.
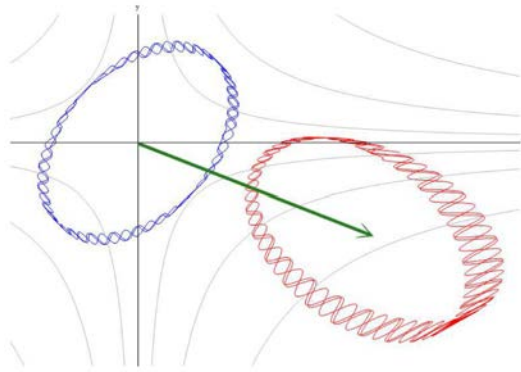
Figure 2.5: Numerically calculated solution to the radial equations of motion with and without offset fields. Taken from [70]. The figure visualizes the increase of micromotion amplitude in the presence of an electric offset field.

Of course, the stability diagram 2.6 is valid only for an ion trap with ideal quadrupole potential. Experimentally, field imperfections caused by electrode geometry lead to the existence of nonlinear resonances. In the stability diagram, these resonances manifest in the existence of lines, where no ions can be trapped. Stability diagrams have been verified experimentally by scanning the trap parameters and measuring the number of trapped ions. For spherical ion traps, results can be found in references [2] and [32]. An example of an experimentally obtained stability diagram where also the lines of nonlinear resonances are visible can be found in figure 2.8. The problem of nonlinear resonances is very well known from accelerator physics.
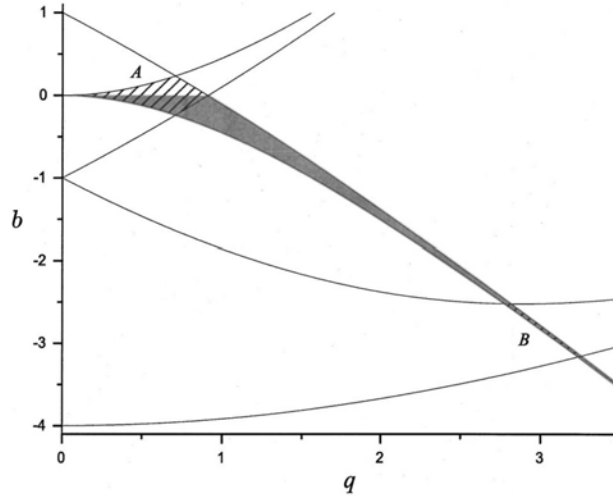
Figure 2.6: Stability diagram for a single ion in a mass filter (hatched area) and in a linear Paul trap (gray shaded area). Taken from [19]. Some features of this diagram can be understood intuitively. These are explained in the text. Although the stable region is infinitely large, Paul traps are typically operated with the parameter q being smaller than 1, in order to keep the micromotion reasonably small. For the mass filter, the voltage contained in the parameter b is an offset voltage on the RF electrodes.

2.1.4   Trap Frequencies

When aiming for quantum mechanical experiments with trapped particles, it is necessary to reduce the number of phonons of the trapped particles such far that quantum behavior becomes important. Even though this is not absolutely necessary for e.g. quantum computing, one would prefer to have particles populating the ground state of the trapping potential. Reducing the number of phonons is done by laser cooling with techniques such as Doppler cooling or Raman sideband cooling. In order to know the temperature which has to be reached for ground state cooling, one needs to know the trap frequencies. From the equations of motion, the axial trap frequency is obviously given by
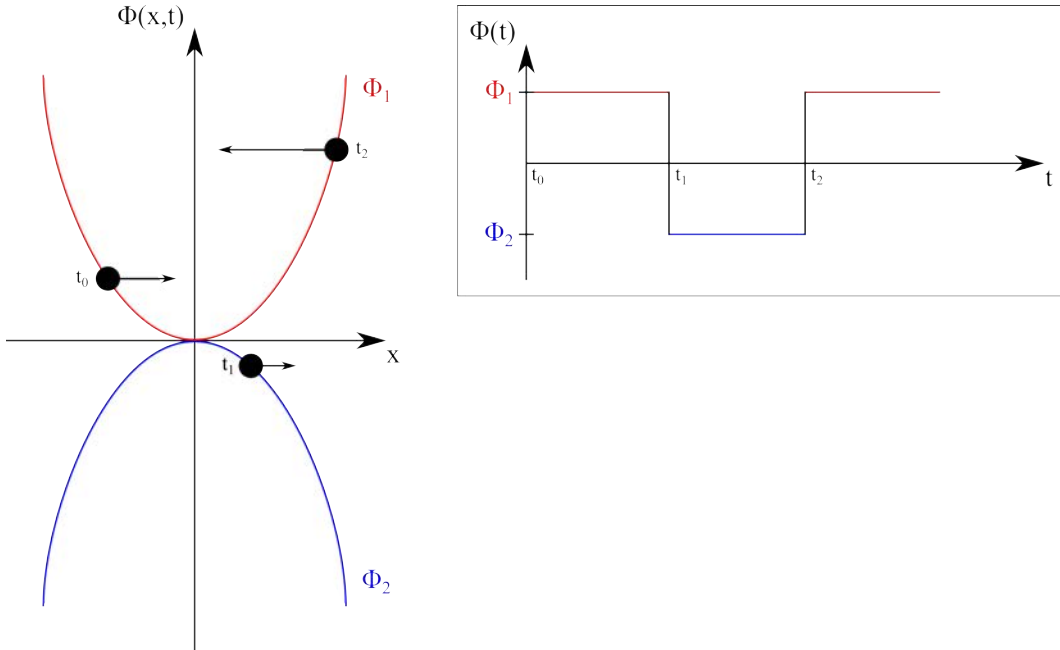
$$\omega_z = \sqrt{\frac{b}{2}}\Omega = \sqrt{\frac{e\alpha V_{cap}}{2mL^2}} \tag{2.7}$$

As reported in [24], the frequency of the radial motion is

$$\omega_r = \frac{\Omega}{2}\sqrt{\frac{1}{2}q^2 - b} = \sqrt{\omega_{r0}^2 - \frac{1}{2}\omega_z^2} \tag{2.8}$$

where

$$\omega_{r0} = \frac{q\Omega}{2\sqrt{2}} \tag{2.9}$$

Figure 2.7: Schematic view of an ion in an oscillating electric field. It visualizes, how a small frequency of field oscillation can cause the motion to be unstable. In other words, the ion is not trapped. This corresponds to the parameter q being too large. Here, the same simplifications mentioned in the caption of figure 2.3 do apply.

It is important to understand that increasing the axial confinement, e.g. by applying a higher end-cap voltage, leads to a weaker radial confinement.

A quantity directly connected with trapping frequency is the potential depth. The potential depth defines the maximum temperature ions can have and still being captured by the trap, even without cooling effects present. Radially, the Paul trap produces an effective harmonic potential with a spatial extend of r_0. Thus, the radial trap depth is given by
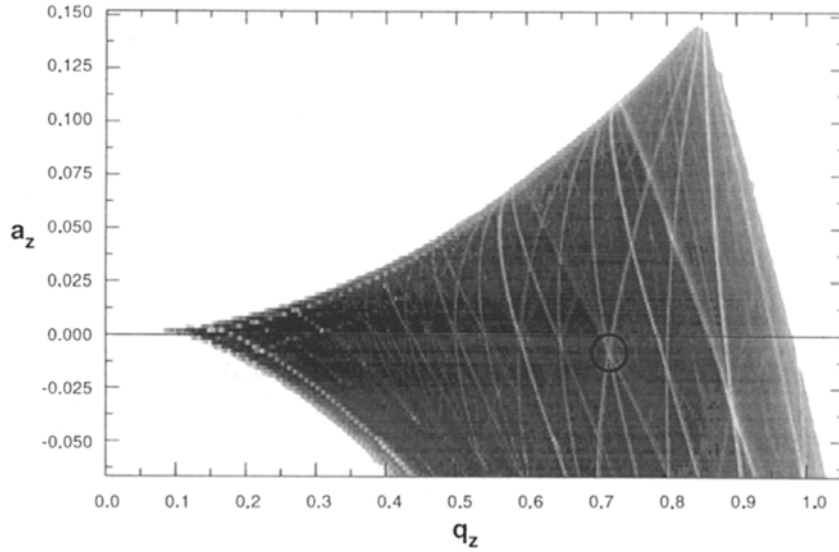
$$U_0 = \frac{1}{2}m\omega_r^2 r_0^2 \tag{2.10}$$

For typical ion traps, the trapping frequencies are on the scale of

$$\omega_r = 2\pi \cdot 1\,\text{MHz}$$
$$\omega_z = 2\pi \cdot 100\,\text{kHz}$$

Disregarding numerical prefactors on the order of 1, the maximum temperature for an ion to be trapped is

$$T_{max} \approx \frac{m\omega_r^2 r_0^2}{k_B} \tag{2.11}$$

Figure 2.8: Measured stability diagram for the spherical Paul trap. Dark regions correspond to high ion number. Lines, where nonlinear resonances occur are clearly visible, as well the outer contour of the stable trapping region. Its shape resembles the one predicted by analyzing of the equation of motion. Taken from [1].

As modern ion traps have electrode spacings of $r_0 \approx 1\,\mathrm{mm}$ and are operated with ions of masses with something like $m = 100u$, typical maximum temperatures are on the order of several thousand Kelvins, even if one assumes the actual trapping volume far smaller than the one defined by the electrode distance.

2.1.5   Nonlinear Resonances

In experimental setups, the electric field deviates in many ways from an ideal quadrupole field. These deviations can be caused by[3]:

- electrode misalignment

- non-hyperbolic shapes

- truncated electrodes

- holes in the electrodes

- space charge potential of a large ion cloud

- influence of potentials from outside the trap

---

[3]This enumeration is a direct quotation from [2].

According to reference [63], where the influence of such deviations on the stability of particle orbits in mass filters was treated, these deviations do not change the dynamics significantly as long as they are occurring non-resonantly. Due to the periodicity in time of the occurrence of these deviations, it is possible that small orbit deviations add up. This is the case, if the ion motion, modeled as a two dimensional harmonic oscillator with frequencies ω_r and ω_z is in resonance with the perturbation. For perturbations caused by the RF electrodes, these themselves occur with the RF drive frequency Ω. Hence, resonant ion loss might be observed, if[4]

$$n_r\omega_r + n_z\omega_z = \nu\Omega \qquad (2.12)$$

where $n_r, n_z, \nu \epsilon \mathbb{Z}$. This does not necessarily mean, for a specific experiment, instability is observed for every possible pair of integer coefficients fulfilling the relation given above. The occurrence of instability depends on the specific type of field error. If one performs a multipole expansion of the ion trap's electric field, the number $N = n_r + n_z$ defines the order of the perturbing field component that leads to resonant instability. Nonetheless, fulfilling the instability relation with low integer coefficients should be avoided.

2.2   Connections with Accelerator Physics

In modern particle accelerators, magnetic quadrupole fields are used for focusing ion beams. The Lorentz force acting transversely on the coasting beam is analogous to the radial Coulomb force in the case of linear Paul traps. In particle accelerators, the magnetic fields have a spatial dependence, whereas in ideal Paul traps, the quadrupole field is time dependent, only. Considering a particle with fixed energy coasting along an infinite FODO structure, this system is related to the case of a trapped ion via a Lorentz transformation. Hence, the systems are equivalent. There is only one obvious difference: In common RF Paul traps, the field oscillates sinusoidally, whereas in accelerators, the magnetic lenses have sharp edges leading to a "digital" alternation between two field configurations. This difference does not falsify the analogy of these two systems: According to [49], it was shown already in 1983 that there is not a significant difference between sinusoidal focusing and FODO quadrupole lattices. Besides, Paul traps can indeed be operated using a rectangular waveform instead of the sinusoidal. These ion traps are sometimes called "digital". An example for such a trapping setup can be found in [7], where the stability diagram is investigated.

    Actually, in the field of accelerator physics, applications exist which make use of the analogy with ion traps. Using ion traps for obtaining a better

---

[4]Taken from reference [2], similarly found for mass filters in reference [63].

understanding of collective phenomena in intense ion beams was proposed in 1999, see reference [15], results published five years later in reference [22]. Additionally, ion traps have been used for simulating effects of magnetic lattice imperfections in references [12] and [49].

Compared with direct beam analysis using an accelerator, using ion traps is advantageous as they

- are cheap.

- are compact.

- do not emit short wave radiation and do not suffer from radio-activation.

- allow for high resolution imaging of the trapped ion plasma.

Chapter 3

Ion Trap Assembly

At first, this chapter explains the design of the electrodes, their mounting structures and the oven design of the ion trap. Afterwards, the generation and delivery of the radio frequency is addressed.

3.1 Ion Trap Design

This section summarizes the ion trap design. It justifies the chosen electrode geometry, materials and machining techniques. Additionally, the electric connections inside the vacuum chamber as well as the oven design are explained.

3.1.1 Electrode Geometry

Several aspects have to be considered when designing an ion trap:

- Although the criterion for the existence of closed orbits inside an ideal Paul trap, which is visualized in the stability diagram 2.6, predicts the possibility to obtain stable motion for every applied RF voltage, it is favorable to choose q around 0.5 in order to avoid nonlinear resonances.[1] Such nonlinear resonances exist due to experimental imperfections. Additionally, the amplitude of micromotion depends on the applied RF voltage quadratically, prompting us to choose V_{RF} reasonably low.

- Quantum experiments with trapped ions benefit from high trapping frequencies, but these cannot be achieved easily. The functional dependency of the radial trapping frequency is

$$\omega_{r0} \propto \frac{V_{RF}}{r_0^2 \Omega}$$

---

[1]Details have been provided in 2.2.

where r_0 is the distance between opposing RF electrodes and Ω is the radio frequency. As V_{RF} scales with the square root of the applied RF drive power, it is not possible to use arbitrarily high voltages. Consequently, for an ion trap with high trapping frequencies, one has to choose a small r_0.

- Imperfections of the electrode surfaces lead to heating effects or even to ion loss, if the ion is trapped very close to the surface. Even if no heating is directly observable, even small imperfections can produce quantum decoherence, complicating the use of stored ions as quantum bits. Thus, very small trap sizes and correspondingly small values of r_0 should be avoided.

- In order to build an ion trap that is ideally modeled by the equations of motion given in chapter 2, one would need to build hyperbolically shaped, infinitely large quadrupole electrodes. These would hamper any optical access, which is necessary for optical manipulation and observation of the trapped ions. Even the schematically drawn ion trap shown in figure 2.4, based on rod-shaped electrodes as has been typically used in the first experiments with linear Paul traps, suffers from this problem. In a setup using rods, the electrodes have to be very close together for the purpose of producing sufficiently strong electric fields.

- A strong axial confinement, i.e. large ω_z , requires high end-cap voltages V_{EC} . These can easily reach several thousands of volts. Such high voltages might not be in compliance with the specifications of the electric vacuum feedthroughs and can massively increase the risk of dielectric breakdowns inside the vacuum chamber. Therefore, the distance L between the end-caps has to be chosen reasonably small.

- A typical problem of ion traps is the existence of unwanted electric stray fields. They cause the trapped ion to be displaced away from the saddle point of the quadrupole field and thereby increase micromotion significantly. Consequently, sources of stray fields have to be avoided by minimizing the amount of dielectric material near the ion trap. Additionally, stray fields must be compensated for by the use of DC electric fields. This can be done by placing additional electrodes near the trap center or by adding an additional DC voltage to each of the quadrupole electrodes.

The electrode design chosen in this experiment has been inspired by the design which was used very successfully in the group of R. Blatt for experiments with ^{40}Ca$^+$ and has been documented in the doctoral thesis of S. Gulde [24]. A slightly modified version has already been successfully used for trapping of Yb$^+$ as reported in reference [70]. An overview of the electrode configuration is depicted in figure 3.1. A technical drawing where all relevant lengths are
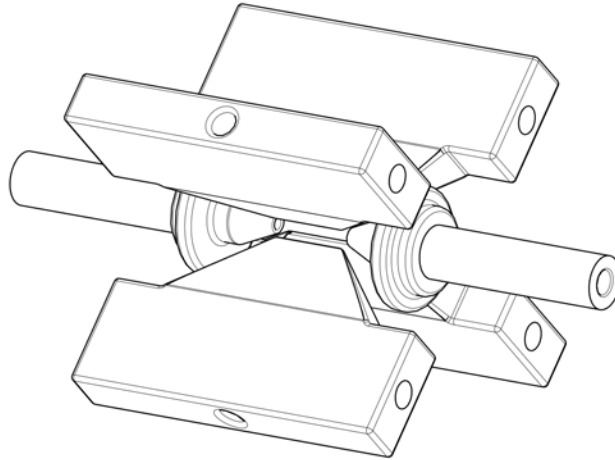
Figure 3.1: The ion trap consists of four blade-like RF electrodes which produce an oscillating quadrupole field and two cylindrical end-caps for axial confinement. Basic advantages of this ion trap design are high trap frequencies and a high degree of optical access. Mounting parts are not displayed in this figure.

denoted can be found in figures 3.2 and 3.3. The spacing between the four quadrupole electrodes is exactly the same as in the Blatt group: $r_0 = 1.6\,\text{mm}$. For producing strong electric fields, the radius of curvature of the electrode tips is only 0.1 mm. The shape of the end-cap electrodes is similar to earlier experiments as well, but a small bore has been added for axial optical access which can also be used for bringing a Bose-Einstein condensate in contact with the trapped ions.

The width of the bore is defined by the constraint that it should be wide enough to allow a 1064 nm laser beam to be sufficiently focused into the trap. Such a Gaussian beam with a focus of, say, 25 µm would be a fine dipole trap if the laser beam is red detuned with respect to a strong transition of the trapped atoms: Potentials of dipole traps are determined by the frequency ω_0 of the relevant internal transition of the atom, the linewidth Γ of this transition, the frequency of the trapping laser and the spatially dependent intensity $I(\vec{r})$ of the light field. In the case of large detunings $\Delta = \omega_0 - \omega$, the dipole potential is given by[2]

$$U_{dip}(\vec{r}) = -\frac{3\pi c^2}{2\omega_0^3}\left(\frac{\Gamma}{\omega_0 - \omega} + \frac{\Gamma}{\omega_0 + \omega}\right)I(\vec{r}) \tag{3.1}$$

To be exact, this expression would have to be multiplied with the multiplicity of the transition. The depth of the trap formed by a focused laser can be estimated if one inserts the intensity in the center of a Gaussian beam for

---

[2]Details on optical dipole traps may be obtained from the review [23].
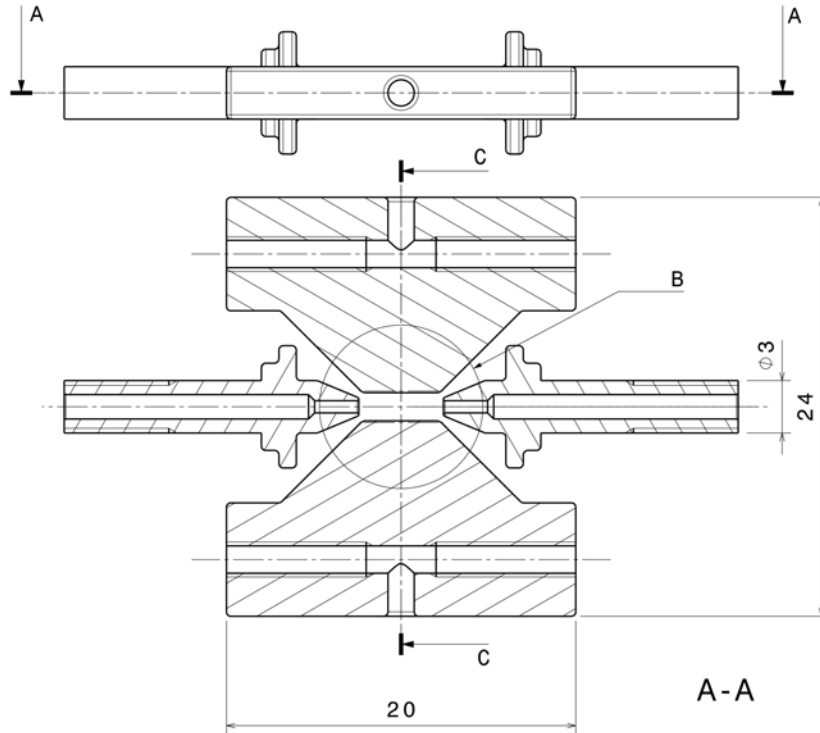
Figure 3.2: Overview of the electrode setup. As one can see from the section view A-A, the quadrupole electrodes have threaded holes, which are required for mounting, as well as a venting bore to reduce the risk of virtual vacuum leaks. Some millimeters away from the trap, the diameter of the end-caps is increased to cover the MACOR parts used for electrode mounting as good as possible. It is advisable to reduce the amount of insulating surfaces near the ion trap as far as possible for avoiding stray fields. Detail B as well as the section view C-C are displayed in figure 3.3.

given laser power P and beam waists w

$$I_{centre} = \frac{2}{\pi w_x w_y} P \qquad (3.2)$$

If one takes, for example, $P = 5\,\mathrm{W}$ of 1064nm light and focuses it down to $w_x = w_y = 25\,\mu\mathrm{m}$, the potential depth for a neutral Yb atom, where the relevant transition has a wavelength of 398.8 nm and a linewidth of 29 MHz , is approximately 100 μK. According to the formula for the waist of a Gaussian beam

$$w(d) = w_0 \sqrt{1 + \left(\frac{d\lambda}{\pi w_0^2}\right)^2} \qquad (3.3)$$

in a distance $d = 25\,\mathrm{mm}$, which is approximately the distance from the center of the trap to the "entrance" of the end-cap, the beam waist has widened to
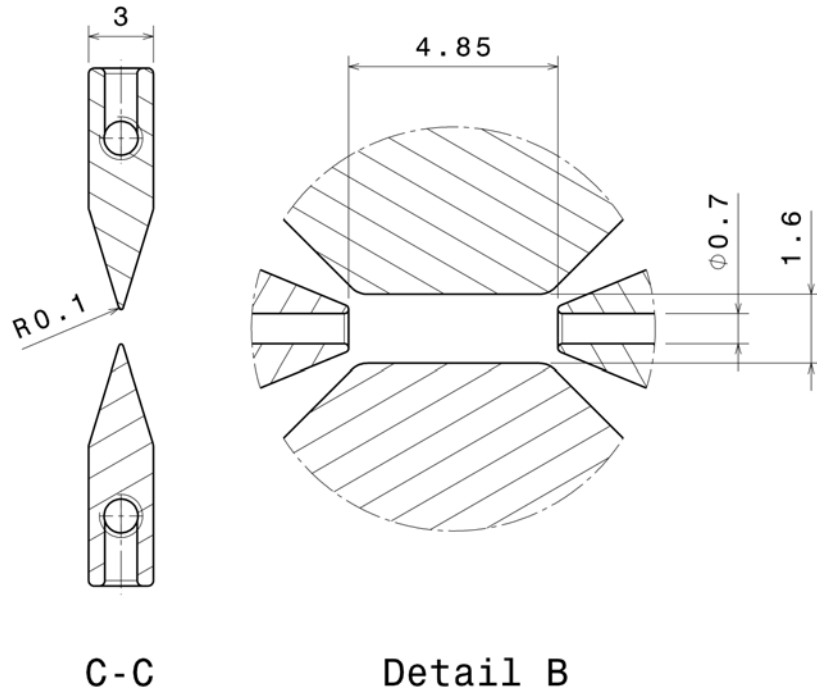
Figure 3.3: Part of the electrode setup that is relevant for the trapping parameters.

0.33 mm. That is the reason why the diameter of the bore has been chosen to be 0.7 mm. For a given end-cap voltage V_{EC} this bore should reduce the axial field component compared with the ion trap of the Blatt group. Hence, the length of the ion trap has been slightly reduced from $L = 6$ mm to $L = 5$ mm .

We have no experience with ion traps and therefore aimed for a very established and reliable design. Besides, the fact that our design is very similar to former designs enables us to make some predictions about parameters for stable motion and trapping frequencies without actually knowing the electric field strengths inside the trap, which could, even if the amplitude of the radio frequency was exactly known, only be calculated numerically.

3.1.2 Electrode Fabrication

Before the production of the ion trap could start, it had to be decided which material should be used for the electrodes, which machining technique would be best and whether any kind of surfaces treatment such as gold-plating or etching would be necessary. The alternatives for the material were stainless steel or a copper alloy. Stainless steel has the advantages that it is comparably cheap and is easily available, compatible with ultra high vacuum without almost any

limitations, can be bought in non-magnetic variants[3] and does not tend to form dielectric oxide layers on its surface. Besides, it has served as electrode material in many other ion trap experiments. The disadvantage of stainless steel is its high electric resistance. As a consequence, heating of the radio frequency electrodes by ohmic resistance is an issue when using stainless steel and limits the applicable radio frequency power.

Concerning electric properties, the best choice would be oxygen free copper. It is also compatible with ultra high vacuum. Yet copper suffers strongly from oxidation and therefore is not usable. Finally we decided to use the alloy beryllium-copper, a material combining both high electric conductivity and low oxidation rate. Unfortunately, the material is expensive and not easily acquired.

The quadrupole electrodes were fabricated by wire erosion technique and milling, whereas the end-caps were made on a lathe. Fortunately, adding the small bore to them has not produced any trouble. All relevant parts of the ion trap have been produced with an accuracy of 0.01 mm. Any deviations from the ideal trap geometry should be small compared to trap dimensions. For pictures of the electrodes taken prior to assembly see figure 3.4 .
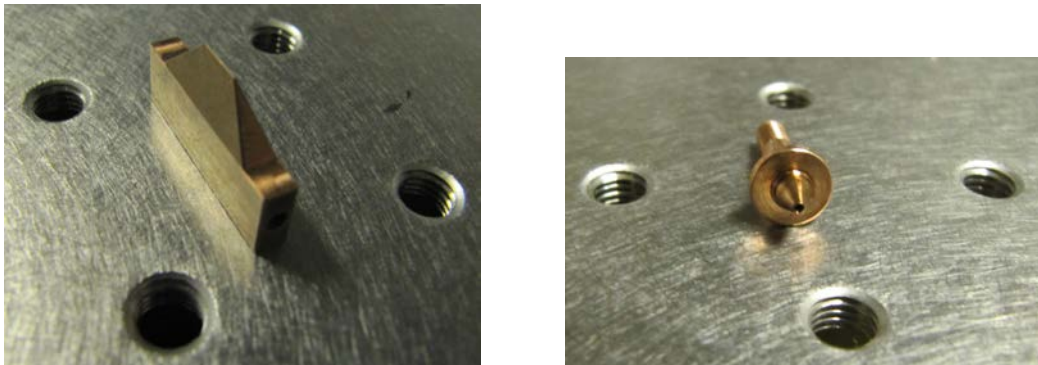
Figure 3.4: Pictures of the electrodes after they came out of the workshop. RF quadrupole electrodes as well as end-caps have been produced from beryllium copper. Due to the limited availability of raw material, the exact composition of the alloy used for the end-caps differs a littler from the one used for the quadrupole electrodes. In these pictures, this manifests in the slightly different colors of the two parts displayed.

Concerning surface treatment, many opinions seem to exist in the ion trapping community. Some say that no treatment is necessary. Others clean and smoothen the surface by etching. Oxidation during assembly is sometimes prevented by gold-plating the electrodes. Even cleaning the edges of the electrodes inside the vacuum with focused high power lasers has been done. We decided

---

[3]For some kinds of experiments, the magnetic field has to be zero or at least well defined.

not to use any surface treatment apart from a thorough cleaning procedure which has to be done for ultra high vacuum applications anyway.

3.1.3 Electrode Mounting

The mounting of the electrodes is done using two parts made from the glass ceramic MACOR. This material combines good mechanical properties with very good electric insulation and vacuum suitability. The parts are shown in figure 3.5. Fixation of the quadrupole electrodes to the ceramic parts is done
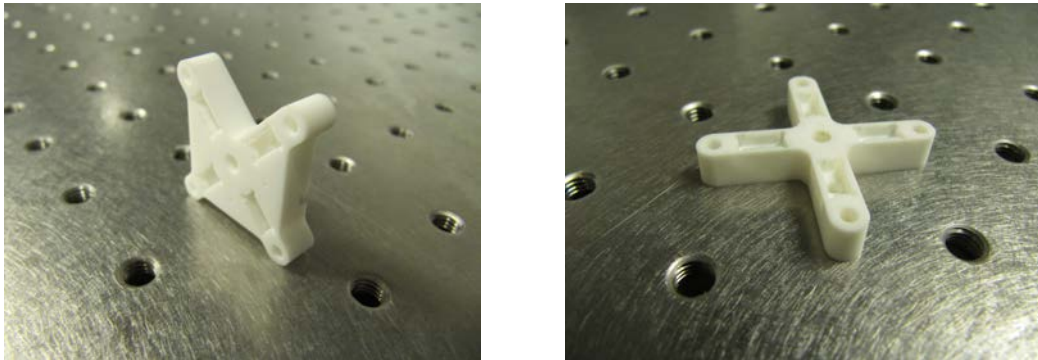
Figure 3.5: Pictures of the MACOR parts that are used for holding the ion trap together. As relative electrode alignment is crucial, the parts have been manufactured with high precision. The amount of MACOR used and consequently the surface area was reduced as far as possible, to avoid for possible sources of electric stray fields. The two mounting parts are not identical, due to the left one containing the collimation holes belonging to the ovens.

by stainless steel screws, which are also used for electric contact. Generally, it is not a good idea to have threads inside an ultra high vacuum. Small amounts of gas trapped inside the thread windings might outgas for a very long time and thereby limit the reachable pressure. In order to avoid this problem, special screws with a lateral longitudinal slot are used. The milling grooves inside the ceramic parts fit exactly to the electrodes and thereby ensure a very exact relative positioning of the electrodes. Mounting of the ion trap inside the vacuum chamber is done using a block made from oxygen free copper (OFHC). This copper block also serves as both thermal and electric ground for three ovens, which are located inside the mounting structure, as described in subsection 3.1.5. An overview of the ion trap assembly is provided in figure 3.6. Figure 3.7 shows the fully assembled and wired ion trap shortly before insertion into the vacuum chamber.

OFHC block

bore for oven

BeCu electrode

MACOR holder
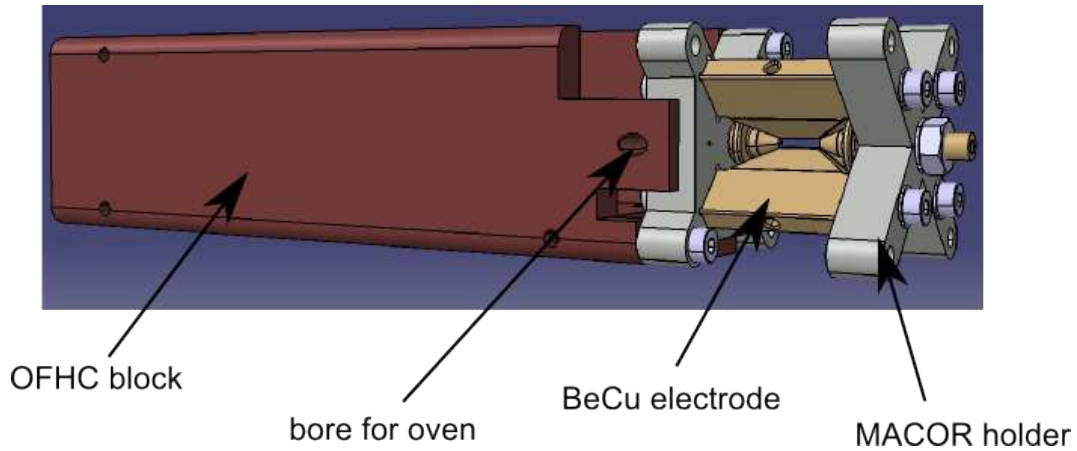
Figure 3.6: CAD sketch of the ion trap. The OFHC copper block is very long, in order to have the ion trap centered in the large vacuum chamber. It is equipped with some threaded holes and venting bores.

3.1.4   Wiring and Electronics in Vacuum

All in-vacuum wiring concerning the electrodes has been done using Kapton isolated, 19-strand, silver plated, oxygen free copper wire[4] with a diameter of 1 mm . A stranded wire is advantageous, because it has a higher conductivity for radio frequency power, due to the skin effect. The skin effect causes the electric current to flow mainly near the surface of the conductor. Consequently, one should increase the surface area. For radio frequency applications, it is especially important to ensure a high conductivity on the surface of the conductor, facilitated here by the silver plating. From a mechanical point of view, stranded wire is advantageous due to its high flexibility. The wires are connected to the electrodes using screws in case of the quadrupole electrodes or nuts for the end-caps, respectively.

In order to ensure phase equality for opposing RF electrodes, it is advisable to interconnect them via a large capacitor, which has a small resistance for radio frequency signals due to the inverse scaling of the impedance with the frequency ω: $|Z| = \frac{1}{\omega C}$. How this connection has been done can be seen in figure 3.8. Additionally, the connections from the electric feedthroughs to the end-caps should be low pass filtered with a very large resistance of some mega Ohm in order to have radio frequency which couples into the end-caps suppressed. These low pass filters are visible in figure 3.9. Hence, it was inevitable to have capacitors and resistors inside the vacuum chamber. Of course, this also required soldering.

All electrical components inside the vacuum chamber are SMD elements. These are surprisingly well UHV compatible. In contrast to electrolyte capac-

---

[4]Kurt J. Lesker FTAKCS10010

itors, SMD capacitors perform well at radio frequencies. All soldered connections inside the vacuum have been soldered with Stannol HF32. It has been chosen because its melting temperature is 227°C, which is higher than that of most other solders and well above the maximum baking temperature of the vacuum system.
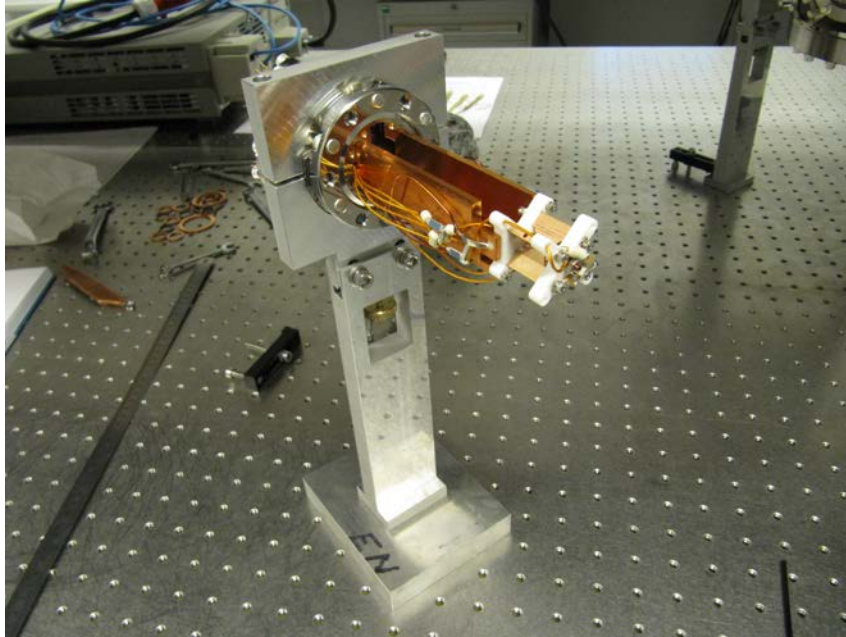
Figure 3.7: Overview of the ion trap assembly shortly before insertion into the vacuum chamber. It is mounted height adjustable and stands stably without being clamped to the optical table, facilitating the insertion.

3.1.5 Ovens and Ionization Scheme

In order to provide trapped ions, neutral atoms have to be evaporated somewhere inside the vacuum chamber and afterwards ionized near the trapping center. Understanding the oven design requires some understanding of the requirements posed by the ionization process, which is discussed first.

There are two common ways of ionizing neutral atoms. One possibility is to use an electron gun to ionize the atoms by electron impact. Another way is to simply shine light of sufficiently short wavelength on the atoms and ionize them by photo-ionization. Of course, this could be done in a one photon process, where one photon, whose energy is higher than the ionization energy of the atom, is absorbed by the atom. Usually this would require photons in deep UV, where good lasers and optics are rare. The better way is a two photon process, where in a first step, the neutral atom gets transferred into an excited state by resonant interaction with a photon and in a second step shortly
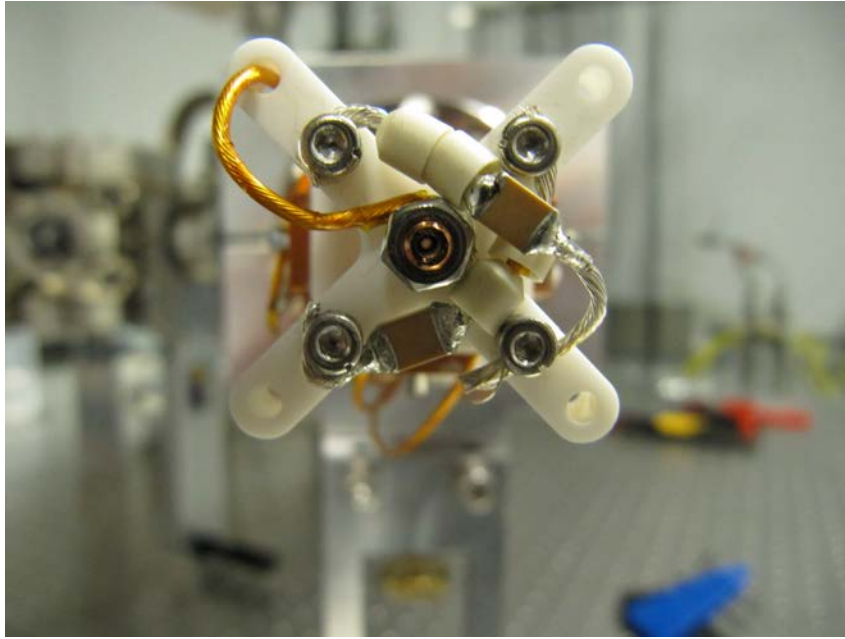
Figure 3.8: Rear side of the ion trap, where the RF electrodes are interconnected via SMD capacitors. Ceramic beads are used for avoiding unwanted electrical contacts.

afterwards absorbs another photon, which ionizes the atom. In contrast to the single photon process, this technique is isotope selective, in the sense that if done correctly, only one isotope out of the natural distribution of isotopes coming from the oven is ionized. As another advantage this process produces no multiply charged ions, in contrast to electron impact ionization. It might as well be considered to be easier from a technological point of view, because the required laser wavelengths are longer. On the other hand, this scheme requires at least one additional narrow-linewidth, resonant laser. The two photon ionization process used in this experiment is visualized in figure 3.10 and in detail explained in the caption.

For future experiments it is desirable to load only one isotope of Yb with high reliability. In order to excite only one isotope of Yb into the state $^1P_1$ it is necessary to have a laser with a linewidth much smaller than lineshifts given in figure 3.11. Additionally, the Doppler shift has to be considered. Velocities of atoms coming from an oven are distributed in a broad Maxwell-Boltzmann distribution. Accordingly, the Doppler shift is different for every atom and can only be coped with by arranging a situation where the Doppler shift vanishes - in good approximation - for all atoms. This condition can be met by ensuring that the 398.9 nm laser is perpendicular on the atom beam emerging from the oven. Of course, this requires the atom beam to be well collimated. To first
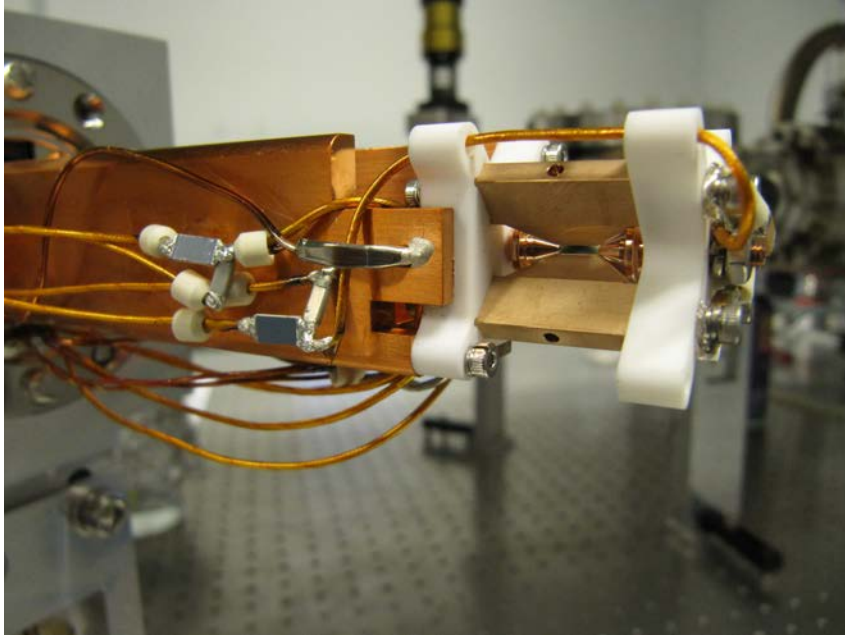
Figure 3.9: In this picture, the two connections for the end-caps together with their low-pass filters are clearly visible. Each filter consists of a 2MΩ resistor and a 22pF capacitor. Next to the low-pass filters, one of the three ovens is located. For securing the press fitted connection between stainless steel capillary tube and copper holder, a small drop of low-outgassing epoxy was added. It was not easy to choose wire lengths appropriately, causing wires to sag. This problem is due to the poorly accessible locations of the electric feedthroughs.

order, the Doppler shift is given by

$$\Delta\omega = -\vec{k} \cdot \vec{v} = -\frac{2\pi}{\lambda} v \cos(\theta) = -\frac{2\pi}{\lambda} \sqrt{\frac{3k_B T}{m}} \cos(\theta)$$

where for the speed v of the atoms the root mean square speed of the Maxwell-Boltzmann distribution has been used. If one assumes the temperature in the oven to be $T = 700\,\text{K}$ the angle θ that produces a Doppler shift of $|\Delta\omega| = 100\,\text{MHz}$ for an atom with mass 174 u is 83°.

The oven design used in this experiment originates from an ion experiment described by M.J. Madsen in his thesis [36], where he filled it with cadmium. He basically took a small piece of stainless steel capillary tube, put a piece of cadmium wire inside, sealed one end of the tube by crimping and attached a power supply to both ends of the tube. Running a current through the tube heats it efficiently, due to the high ohmic resistance of stainless steel - as compared to copper. The open end of the tube is directed at the experiment delivering a well collimated atomic beam. Cadmium is a metal with a quite low melting point of $T = 594\,\text{K}$ and an accordingly high vapor pressure for a given temperature. For example, the temperature where a vapor pressure
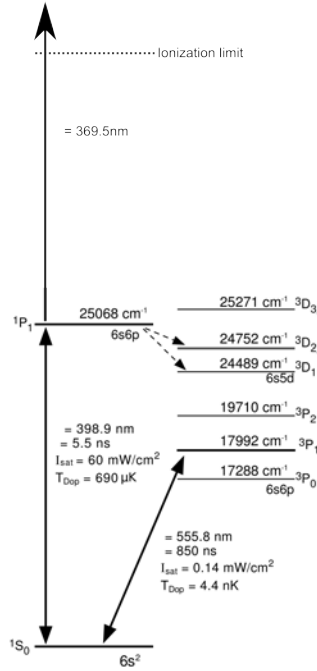
Figure 3.10: Level scheme for the lowest levels in ytterbium. This is a modification of a figure found in reference [37]. The neutral ytterbium atoms are excited from their ground state $^1S_0$ to the excited state $^1P_1$ using a 398.9 nm laser. This process is isotope selective. The necessary laser frequency differs from isotope to isotope by some 100 MHz, as can be seen in figure 3.11. A second photon, which originates from the same laser used for cooling and manipulating the ions and has a wavelength of 369.5 nm is used to ionize the excited neutral atom. The ionization limit for a neutral atom in the state $^1P_1$ is roughly 394 nm.

of $p_{vap} = 1$ Pa is reached[5] is $T = 530$ K. For Ytterbium, these values are significantly higher: Ytterbium melts at $T = 1097$ K and the temperature for a vapor pressure of $p_{vap} = 1$ Pa is $T = 736$ K. These differences require Madsen's design to be modified in two ways, in order to make is usable as an Ytterbium atomic source:

- Accounting for the higher operating temperature and our high requirements considering beam collimation, an additional collimation is provided by a narrow 0.5 mm wide and approximately 5 mm long collimation hole within between oven and ion trap. This collimation hole is simply realized by a bore inside the ceramic part which serves as a mount for the trap electrodes. During trap operation, the temperature of this ceramic part should only increase by a few Kelvin and therefore always be far colder than the oven itself.

---

[5]Melting points and vapor pressures are listed in [34].

| Isotope	Shift from ^{174}Yb (MHz)				
	This work	Ref. [7]	Ref. [13]	Ref. [11]	Ref. [19]
^{176}Yb	-509.98 ± 0.75	-507.2 ± 2.5		-509.4 ± 4.0	-469.2 ± 2.7
^{173}Yb $(F = 5/2)$	-254.67 ± 0.63				
^{173}Yb $(F = 3/2)$	516.26 ± 0.90				
^{172}Yb	533.90 ± 0.70	527.8 ± 2.8		529.9 ± 4.0	530.20 ± 7.80
^{173}Yb $(F = 7/2)$	589.00 ± 0.45	578.1 ± 5.8			
^{171}Yb $(F = 3/2)$	833.24 ± 0.75	832.5 ± 5.6	834.4 ± 4.0		
^{171}Yb $(F = 1/2)$	1152.86 ± 0.60	1151.4 ± 5.6	1136.2 ± 5.8		
^{170}Yb	1192.48 ± 0.90	1175.7 ± 8.1	1172.5 ± 5.7	1195.0 ± 10.8	1158.9 ± 11.4
^{168}Yb	1886.57 ± 1.00		1870.2 ± 5.2		
^{173}Yb (centroid)	291.61 ± 0.35			291.2 ± 10.0	
^{171}Yb (centroid)	939.78 ± 0.54	938.8 ± 4.2	935.0 ± 3.3	943.7 ± 7.0	

Figure 3.11: A list of isotope lineshifts for the transition between $^1S_0$ and $^1P_1$ in Yb with respect to the line in the most abundant isotope^{174}Yb. Taken from reference [4].

- Constant heating of the oven to a sufficiently high temperature would increase the temperature of the surroundings significantly. Additionally, constant oven operation is not acceptable if it is situated very close to an experiment requiring - or at least benefiting from - ultra high vacuum conditions with a pressure in the range of 1×10^{-11} mbar. Instead, we decided to use the oven in pulsed operation, where it is heated by running 100 A through it for approximately 100 ms.

These modifications have been adopted from the thesis of C. Zipkes [70], where some estimates for the oven temperature increase can be found which should basically apply here. As atomic source a piece of Ytterbium wire had to be bought, which was not easy to come by. Using far cheaper powder instead was not a possible. It would not have stayed inside the tube and in the worst case would have clogged the collimation hole. Finally, a wire with square profile and an edge length of 1 mm has been bought. The capillary tube has been chosen in such a way that the wire fits exactly into it. A 1.5 cm long piece of capillary tube with an outer diameter of 2.0 mm and an inner diameter of 1.4 mm has been used for each of the ovens. The length of the ytterbium wire is approximately 4 mm. Electric connection is provided by a Kapton isolated OFHC wire with a diameter of 1 mm. The wire is attached to the stainless steel capillary tube by crimping, which should also seal the oven sufficiently. As the risk of melting the Ytterbium piece is considered quite low due to pulsed heating and the high melting temperature, the lengthy sealing procedure described in reference [36] has not been applied. Attaching the oven to the OFHC block was done by press fitting. A small drop of UHV compatible epoxy [6] has been used in order to ensure that the oven stays fixed even if handled roughly. The oven setup is visualized in figure 3.12. Although

---

[6]MDC UHVGLUE-H27D

the temperature around the oven is expected to rise only by about a tenth of a Kelvin after firing, the ion trap is equipped with two PT100 thermistors located near the ovens. These temperature sensors could be useful to understand thermalisation of the experiment and may indicated a malfunction of an oven. They are glued to the copper block using the vacuum glue mentioned before. Deciding on an appropriate number on ovens and finding good positions for them was a decisive process during the design. Finding the positions had to be done with respect to optical access orthogonally to the atomic beams and therefore cannot be clearly distinguished from the vacuum design. In former experiments of other groups, this kind of oven was reported to be very reliable and long lasting. Nonetheless, we decided to have three identical ovens, in order to account for our lack of experience with this oven design and as a precaution for the case that the ytterbium in one of the ovens should become depleted after some time.
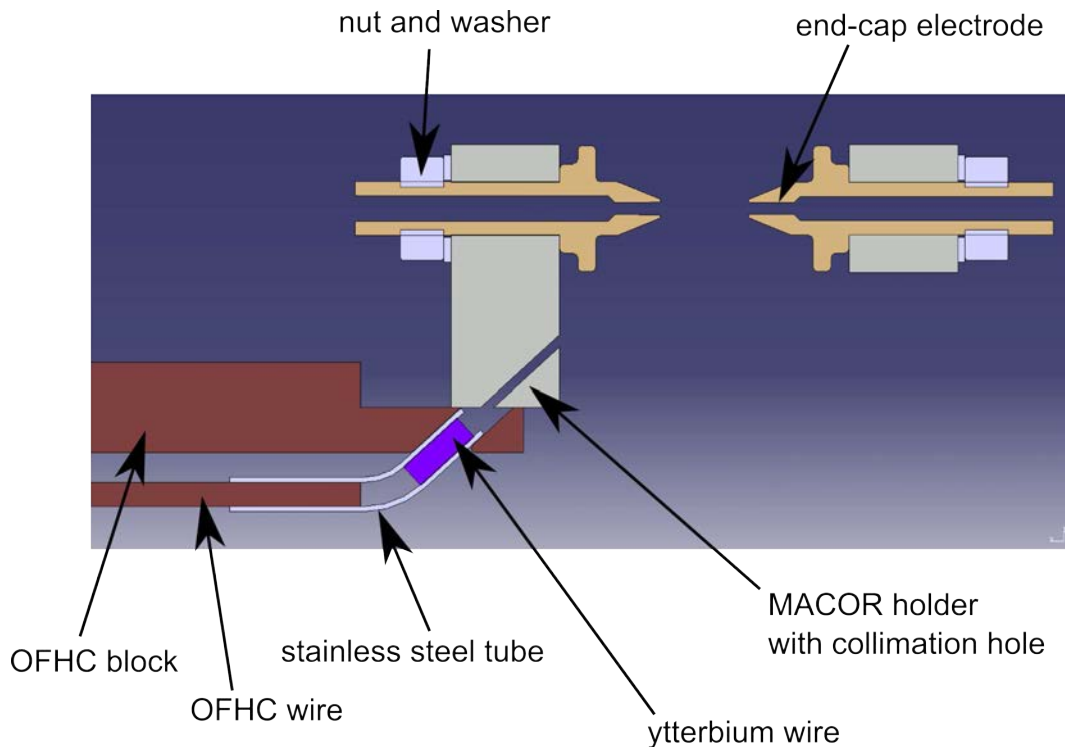
Figure 3.12: CAD drawing of the oven section.

As power supply for the ovens, it was decided to use lead batteries. They are cheap and support very high currents. Initially it was tried to use a speed controller usually used in model making for controlling the high current. This did not work too well, due to the low resistance of the oven and short circuit protections typically present in commercially available speed controllers. Johannes Thielking designed a circuit based on MOSFETs capable of controlling the current. It is also equipped with hard wired as well as software based

interlocks aiming to avoid destruction of the ovens or premature depletion of the ytterbium. Details on the oven firing electronics are going to be presented in J. Thielking's upcoming master thesis.

3.2 RF Generation

For the purpose of trapping atomic ions for quantum experiments, a radio frequency with an amplitude of several 100 V and some mega Hertz is necessary. A common technique to produce these high amplitudes using RF amplifiers with several Watt is to build a resonant circuit consisting of the ion trap and a so called "helical resonator". These resonators are very well known from their application as band pass filters in radio communication systems. Their filtering behavior also reduces the noise injection into the ion trap. A disadvantage of using helical resonators is that the frequency at which the ion trap can be operated is determined by the design of the resonator and cannot be tuned easily.

To begin with, it is useful to understand why generating the RF is not done by simply attaching a large amplifier directly to the ion trap. In such a simple scheme, the power P would be delivered by a coaxial cable with an impedance of $50\,\Omega$. The impedance of the ion trap is much larger than that. Assuming no ohmic resistance to be present, the impedance is given by

$$|Z| = \left| \omega L - \frac{1}{\omega C} \right|$$

where ω is the applied frequency, L is the inductance and C is the capacitance of the ion trap. Modeling the ion trap to be composed of four cylindrical rods with length $l = 15\,\mathrm{mm}$, distance $d = 1.6\,\mathrm{mm}/\sqrt{2}$ and radius $R = 0.1\,\mathrm{mm}$, one obtains for neighboring pairs of electrodes

$$C = \frac{\pi \epsilon_0 l}{\cosh^{-1}\left(\frac{d}{2R}\right)} = 6 \times 10^{-14}\,\mathrm{F}$$

and

$$L = \frac{\mu_0 l}{\pi} \cosh^{-1}\left(\frac{d}{2R}\right) = 5 \times 10^{-9}\,\mathrm{H}$$

For obtaining the values of the entire RF electrode arrangement, these values have to be multiplied by a factor of four. With $\omega = 15\,\mathrm{MHz}$ the impedance is calculated to be $|Z| = 46\,\mathrm{k\Omega}$. Considering the huge difference in impedance between cable and trap, almost none of the applied RF power would reach the ion trap, as it would be reflected at the end of the coaxial cable. Hence, the most important task of the helical resonator setup typically used in ion trap experiments is to match the impedances of amplifier and ion trap.

A helical resonator is shown in figure 3.13. It consists of a coil mounted in a tube, both made from highly conducting material with ideally clean surface. The tube is commonly referred to as "shield" because it is connected to the ground. The open end of the coil is the output of the resonator. Coupling radio frequency into the resonator can be done by either connecting the source directly to the coil or by using an antenna which is also placed within the shield. The latter is used in this experiment, because this simplifies impedance matching between amplifier and resonator.

In this experiment, the radio frequency is provided by a signal generator[7] and a broadband amplifier[8].

3.2.1   Helical Resonator Design

In the following, the design guidelines for helical resonators are given and explained. This subsection summarizes information given in references [35],[58] and [24]. The symbols are explained in figure 3.13.
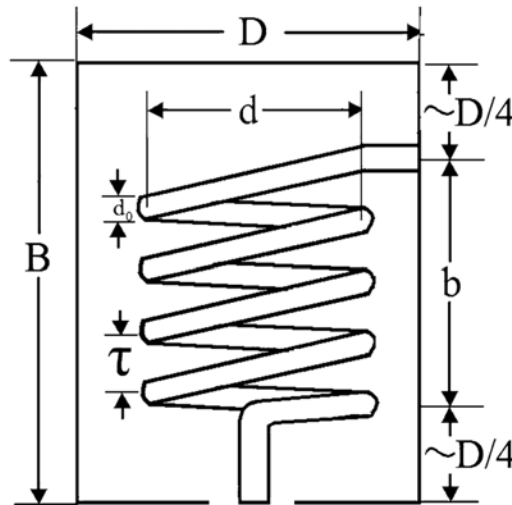
Figure 3.13: Schematic drawing of a helical resonator with all relevant dimensions. Taken from [58].

The following design guidelines for helical resonators are to a large extend found empirically and are given without any explanation:

- The (lowest) resonance frequency is given by $\nu_0 \approx \frac{2670}{N \cdot d}$MHz $\cdot$ cm where N is the number of windings.

- For achieving a high quality factor Q, the following conditions should be met:

---

[7]HP 8656B
[8]Mini-Circuits LZY-22+, 30W

- $d/D = 0.55$
- $1 < b/d < 4$

- The quality factor for well designed resonator is given by

$$Q = \omega_0 \frac{energy\ stored}{power\ dissipated} \approx 20D\sqrt{\nu_0/\mathrm{MHz}}\,\mathrm{cm}^{-1}$$

According to these rules, a helical resonator with a resonance frequency of about 15 MHz was to be build. This frequency was aimed at, because our entire ion trap geometry is very similar to an ion trap once build for $^{40}\mathrm{Ca}^+$. This ion trap was operated successfully at about 30 MHz. In order to work in the same region of the stability diagram - assuming comparable RF voltage amplitude - the RF frequency had to be reduced by a factor of two. This compensates for the mass of ytterbium, which is about four times the mass of calcium. For a helical resonator, a frequency of 15 MHz is comparably low, leading to large dimensions if a high quality factor is aimed for. Limited by the availability of copper tube for the shield and by the fact that the copper wire used for the coil should be bend by hand, a helical resonator with the following dimensions was constructed:

- $B = 290\,\mathrm{mm}$

- $D = 180\,\mathrm{mm}$

- $b = 200\,\mathrm{mm}$

- $\tau = 10\,\mathrm{mm}$

- $d = 100\,\mathrm{mm}$

- $d_0 = 5\,\mathrm{mm}$

Accordingly, the resonator is expected to have a resonance at $\nu_0 \approx 13.5\,\mathrm{MHz}$ and a quality factor of $Q \approx 1300$. As the coil is quite large and not very stiff, a support structure made from plastics had to be build. This support structure is expected to lower the resonance frequency as well as the quality factor. In order to keep these negative effects small, a minimum amount of plastics is used for the support structure, see figure 3.15.

After the assembly was finished as described in subsection 3.2.2, the resonance frequency was measured using a network analyzer. This measurement yielded that the resonator has a spectrum of equidistant resonances, with the lowest one occurring at a frequency of 11 MHz. While the reduction of resonance frequency can be explained by the coil support structure that has not been taken into account during the design process or by other imperfections

such as a slightly larger coil diameter, the occurrence of higher harmonics was unexpected. This behavior has to best of our knowledge not been reported in radio engineering publications, but it is known by other ion trapping groups and can be a problem, if a noisy radio frequency generator is used. Here, it was aimed at understanding helical resonators at least a little bit better.

Electrically, a helical resonator is basically characterized by the capacity of the shield C_S, the capacity of the coil C_C and the inductance of the coil L_C. According to reference [58], these quantities are approximately given by

$$
\begin{aligned}
C_S &= 39.37 \cdot \frac{0.75}{\log_{10}\left(\frac{D}{d}\right)} \cdot b \cdot 10^{-12} \frac{\text{F}}{\text{m}} \\
C_C &= \left(11.26 \cdot \frac{b}{d} + 8 + \frac{27}{\sqrt{\frac{b}{d}}}\right) \cdot d \cdot 10^{-12} \frac{\text{F}}{\text{m}} \\
L_S &= 39.37 \cdot \frac{0.025 d^2 \left(1 - \left(\frac{d}{D}\right)^2\right)}{\tau^2} \cdot b \cdot 10^{-6} \frac{\text{H}}{\text{m}}
\end{aligned}
\qquad (3.4)
$$

It might be useful to compare the values with other capacities and inductances occurring in the RF system. The values for our resonator are:

$$
\begin{aligned}
C_S &= 23\,\text{pF} \\
C_C &= 5\,\text{pF} \\
L_C &= 14\,\text{µH}
\end{aligned}
$$

Naively, one could assume the helical resonator to be a simple LC-circuit. In our case, this would have a single resonance at

$$
\nu_0 = \frac{1}{2\pi\sqrt{LC}} = \frac{1}{2\pi\sqrt{(C_S + C_C)\,L_C}} = 8\,\text{MHz}
$$

This deviates substantially from the value expected from the design calculations. For a better understanding of helical resonators, they have to be considered as - to speak in terms of an appropriate mechanical analogue - vibrating strings, where one end of the string is fixed and the other moves freely. In this analogue, the longest possible standing wave has a wavelength of $\lambda = 4L$ where L is the length of the string. Higher harmonics occur for $\lambda = \frac{4L}{n}$ where n is an odd natural number. This mechanical analogue is reasonable, because one end of the coil is connected to the shield, which itself is connected to the ground, while the instantaneous potential at the other end of the coil can in principle have any value. As these considerations are aiming at calculating resonant frequencies, it has to be taken into account how frequencies and wavelengths are

connected for given speed of wave propagation: $\nu = \frac{c}{\lambda}$. The speed of propagation for electromagnetic waves in conductors with non-negligible capacitance and inductance is given by

$$c_0 = \frac{1}{\sqrt{\hat{L}\hat{C}}}$$

where $\hat{L}$ and $\hat{C}$ are the linear densities of inductance and capacitance. The lowest resonance should accordingly have the frequency

$$\nu_0 = \frac{1}{4\sqrt{LC}}$$

Interestingly, the length of the coil drops out of the calculation. With the given values one obtains

$$\nu_0 = 12.6\,\text{MHz}$$

which seems to be consistent with values calculated at the beginning.

3.2.2 Helical Resonator Assembly

All conducting components of the helical resonator were made from high conductivity copper. Prior to final assembly, all inner surfaces have been thoroughly cleaned using citric acid. Silver plating the relevant surfaces is in principle useful, but has not been done. The shield has a wall width of $10\,\text{mm}$, which makes it immensely heavy (about $20\,\text{kg}$) and expensive. Using this copper tube was not easy to avoid: In order to achieve a high quality factor the shield should not have a seam. As a low electrical resistance of all connections is important for having a large quality factor, the coil is soldered to the shield. This soldering turned out to be a very lengthy procedure, because soldering two parts together requires them to be both heated above the melting temperature of the solder. The shield had to be heated using a blowtorch for about an hour, until a temperature of about 200°C was reached. After the parts were soldered together, they were cooled with water in order to have the solder cured faster. Copper reacts with air when heated above a certain temperature and the torch had blackened some parts of the resonator with soot, making a tedious cleaning procedure necessary. A photo taken during soldering can be found in figure 3.14.

The supporting plastic structure has been 3D printed. It consists of two identical parts plugged into both openings of the coil and connected with plastic screws. It has three mechanical tasks which it fulfills very well:

- It ensures the radial positioning of the coil with respect to the shield.

- It dampens vibrations of the coil.

- It adjusts the correct length and winding pitch of the coil.

Figure 3.14: Picture taken during soldering. A piece of copper wire is soldered to the shield using an blowtorch.

Of course, it has not been added to the setup until soldering and cleaning was finished. Figure 3.15 shows the finished resonator moments before it was closed with the second cap, which also carries the antenna (see figure 3.16).

To account for the large mass of the helical resonator, a very stable mount has been constructed from aluminum, similar to the mount used for the ion pump. In order to decrease the fraction of radiated RF power, the resonator is located only 50 cm away from the ion trap. Although a further decrease of this distance would be preferable, this is not possible due to the resulting reduction of axial optical access to the vacuum chamber and the ion trap.

3.2.3   Connection to Paul Trap and DC Offsets

A very obvious question one stumbles upon before connecting the resonator to the Paul trap is: What kind of wiring should be used? Efforts to decrease the radiated RF might lead to using common $50\,\Omega$ coaxially shielded cable. This is a very bad idea. To understand this, two aspects have to be taken into account:

- Radio frequency gets reflected if the impedance of the conductor changes. As the impedance of neither the ion trap nor the helical resonator is expected to be $50\,\Omega$, serious loss of radio frequency power would occur.

- The resonant frequency of the total system comprising ion trap, connections and helical resonator is lower than that of the helical resonator alone. According to reference [24] good results for the resonance of the loaded resonator are found when using the following model:

    – The "extension" of the resonator consisting of ion trap, wires and feedthroughs can be treated in the same way the helical resonator
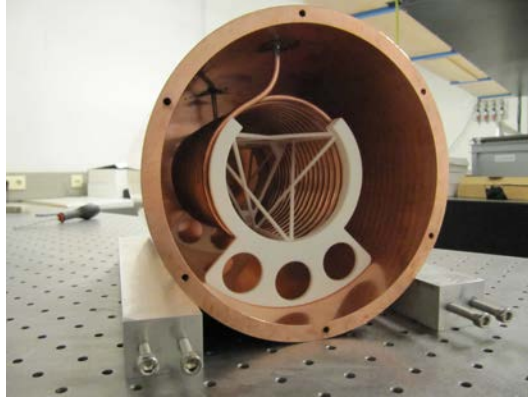
Figure 3.15: Finished helical resonator. The output cap on the rear side is already attached. The white support structure was 3D printed. The material is a polyamide. In principle, having isolating material inside the helical resonator should be avoided. Here, having a support structure could not be circumvent because the coil lacks stiffness. In order to avoid negative effects of the support structure on the electric properties of the resonator, the amount of plastics was minimized. Additionally, the support structure was mechanically designed in such a way that the inductances and capacitances given in formula 3.4 are expected to change only slightly.

was treated. Their capacitance and inductance, more or less continuously distributed, lead to a phase velocity via the formulas given in subsection 3.2.1 and via a $\lambda/4-$condition to a resonance frequency ν_2.

– The frequency of the lowest resonance of the total system is again given by a $\lambda/4$- condition. Using the symbols defined in figure 3.17, one can define an average velocity c for an electromagnetic wave traveling through the circuit:

$$c = \frac{l_0 + l_2}{\frac{l_0}{c_0} + \frac{l_2}{c_2}}$$

where c_0 and c_2 are the phase velocities for waves traveling along the helical resonator or along the extension, respectively. The lowest order $\lambda/4$-resonance for the combined system is given by

$$\nu = \frac{c}{4\,(l_0 + l_2)} = \frac{1}{4\left(\frac{l_0}{c_0} + \frac{l_2}{c_2}\right)}$$

Using the $\lambda/4$-conditions for the helical resonator $\frac{4l_0}{c_0} = \frac{1}{\nu_0}$ and for the extension $\frac{4l_2}{c_2} = \frac{1}{\nu_2}$ yields:

$$\frac{1}{\nu} = \frac{1}{\nu_0} + \frac{1}{\nu_2} \tag{3.5}$$
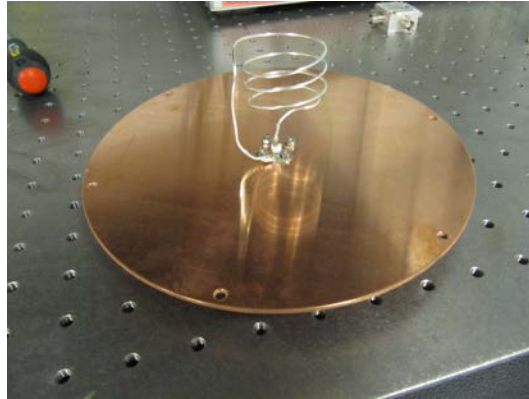
Figure 3.16: Input cap with small coil serving as antenna. The parameters of this antenna are adjusted by trying in such a way that the radio frequency couples most efficiently to the resonance of the system formed by helical resonator and ion trap.

where ν_0 is the resonance of the unloaded helical resonator.

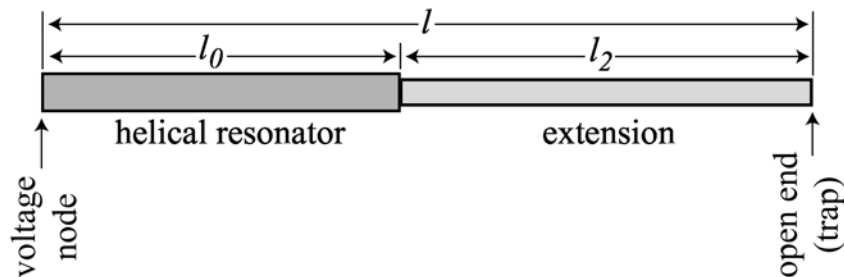**Figure 3.17:** Simple model for the combined system of helical resonator and extension. The left end of the circuit is connected with ground and corresponds - in the mechanical analogue - to the fixed end of the string. At the other end of the circuit, the ion trap is located. Here, the instantaneous voltage can in principle obtain any arbitrary value. For coupling RF power into this circuit efficiently, a $\lambda/4$-resonance condition has to be fulfilled. This is explained in the text. Taken from [24].

Obviously, if the ion trap is to be operated at frequencies of about 10 MHz, ν_2 should be large. Therefore, the capacitances and inductances of the extension should not be significantly large than those of the helical resonator. It was decided to use unshielded multiple strand copper wire for connecting the helical resonator to the electric feedthroughs.

Another aspect complicating the RF setup is the necessity to apply DC voltages of some volts directly to the radio frequency electrodes. Radio frequency power coupling into the voltage supplies used for DC offsets could pose

a serious problem. In order to avoid this, highly attenuating first order low-pass filters are put in between the DC offset voltage sources and the radio frequency electrodes. This is done for all four RF electrodes, although only two of them are actually connected to the RF source in our driving scheme. In order not to short-circuit the voltage supplies, they are decoupled using capacitors. Assembled helical resonator and the RF delivery section are shown in figure 3.18. The low pass filters are located inside the large gray box attached to the resonator mount. Next to this box, a smaller box is located, containing two high voltage sources[9] supplying the end-caps. These have analog control and are capable of producing up to $2\,\mathrm{kV}$.
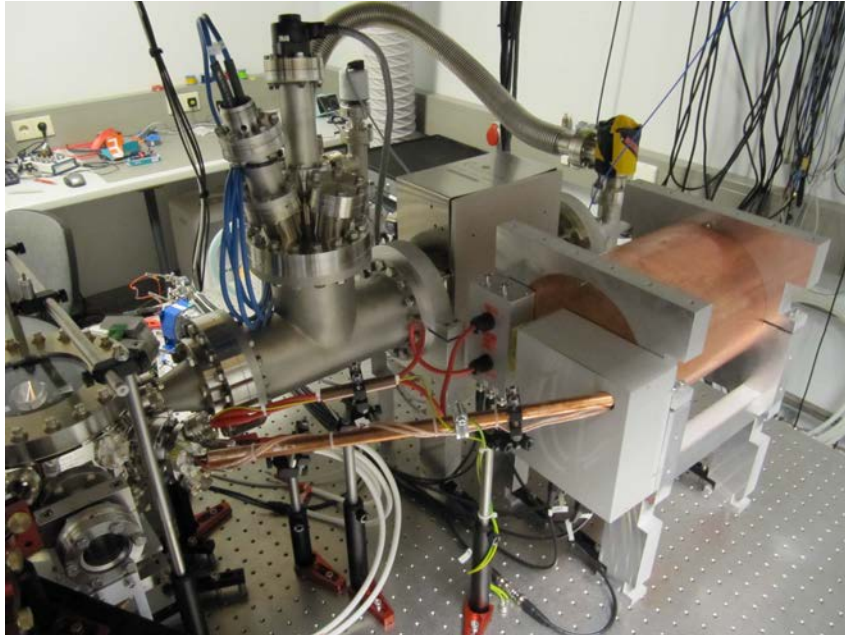
Figure 3.18: Picture of the experiment after the ion trap had been brought into vacuum and all electric feedthroughs have been cabled. The wires are located inside, respectively wrapped around, a copper pipe, for mechanical reasons. Also visible is the box containing the high voltage sources.

After the helical resonator was connected to the ion trap, the input antenna had to be optimized to allow for a maximum of power coupled into the resonator. This was done using a network analyzer again. Finally, more than 99% of applied RF power could be coupled into the system, using an antenna with two windings, a diameter of $40\,\mathrm{mm}$ and a winding pitch slightly larger than $15\,\mathrm{mm}$. This coil was wound by hand and optimizing the coupling was performed just by slightly bending it again and again. That is why exact dimensions of the antenna finally used cannot be given.

---

[9]iseg BPp 20 504 5

Surprisingly, the lowest observable resonance of the total system was at about 30 MHz instead of the expected 10 MHz. Higher harmonics have been observed, but coupling was optimized for the lowest one. A very weak resonance was observed below 5 MHz but coupling could not be optimized satisfactorily for this one. We do not understand this behavior completely. Most likely, we are coupling to one of the higher harmonic resonances while the lower resonances are suppressed.

Chapter 4

Vacuum System

4.1 Vacuum Design

Designing the vacuum system and positioning the ion trap inside the vacuum system was the first step of the experiment design. During this process it had to be ensured that

- the ion trap is optically accessible along the relevant axes.

- high resolution imaging and ion addressing is not hampered by low numerical aperture.

- the experiment chamber is sufficiently pumped.

- the setup is mechanically stable but easily assembled.

- a possible extension of the experimental setup for an experiment which combines trapped ions with Bose-Einstein condensates would be feasible.

Constraining aspect of the experiment design was that some components like the vacuum chamber and suitable viewports had already been bought two years before the start of the project.

4.1.1 Experiment Chamber

The part of the vacuum chamber where the experiment takes place is a commercially available "Extended Octagon" produced by Kimball Physics[1]. It is equipped with two CF160 (8"CF), eight CF40 (2.75"CF) and 16 CF16 (1.33"CF) sealing surfaces[2]. All sealing surfaces are oriented towards the center

---

[1]MCF800-ExtOct-G2C8A16

[2]There is a little but confusing difference between metrical and imperial flange specification: The measure in the imperial system describes the outer diameter of the flange, whereas in the metrical system, the inner diameter is used for specifying a CF flange.

of the chamber and are placed in opposing pairs. In addition to the vacuum chamber, two CF160, eight CF40 and eight CF16 viewports have been bought from Larson Electronic Glass. They have large view diameters, fused silica glass with a surface quality of lambda/4 and are bakeable up to 200°C. Using fused silica is necessary because it is one of the few materials with acceptable transmission in the UV spectral range.

With this equipment one could in principle have optical access along nine axes through the center of the chamber. Consequently, it seems easiest to center the ion trap in the experiment chamber. Nonetheless, at the beginning of the design process, it has been tried whether it would be possible to locate the ion trap outside the center of the chamber, in order to have space for building a magneto-optical trap (MOT) adjacent to the ion trap. After some CAD based tests it was concluded that this could in principle be feasible, but worsens optical access to the ion trap significantly, so the idea was abandoned. For such purposes one would have had to design a custom made vacuum chamber. This would have taken at least a month and also complicated other design aspects. An important aspect for finding an appropriate position for the ion trap was the requirement to be able to shine laser light orthogonally on each of the atomic beams emerging from the ovens had to be ensured. Additionally, one laser oblique with respect to each of the three trapping axes is needed to facilitate laser cooling. This enables us to use a single laser for Doppler cooling of all three motional directions.

Another disadvantage of the vacuum chamber with respect to optical access is that it is very large, causing the ion trap to be far away from the windows and thereby limiting the reachable optical resolution, as explained in section 5.2. Solving this problem by a displacement of the ion trap away from the center of the vacuum chamber was not an option because of the resulting limited optical access along other axes than the z-axis.

4.1.2   Trap Mounting and Feedthroughs

After the decision on the trap position and orientation inside the vacuum chamber had been made, solutions for its mounting and for the wiring of the electrodes, ovens and temperature sensors had to be found. One design guideline was to have the possibility to add and remove the ion trap easily from the rest of the vacuum system. This enables us to compare the behavior of the vacuum system before and after insertion of the trap. In case of serious vacuum problems, they can be more easily located, especially concerning outgassing of material or virtual leaks in the trap assembly. Besides, it would facilitate changes in the trap design, if they should become indispensable.

The copper block on which the trap is mounted is attached to the vacuum chamber using mounting items provided by Kimball Physics. As the chamber
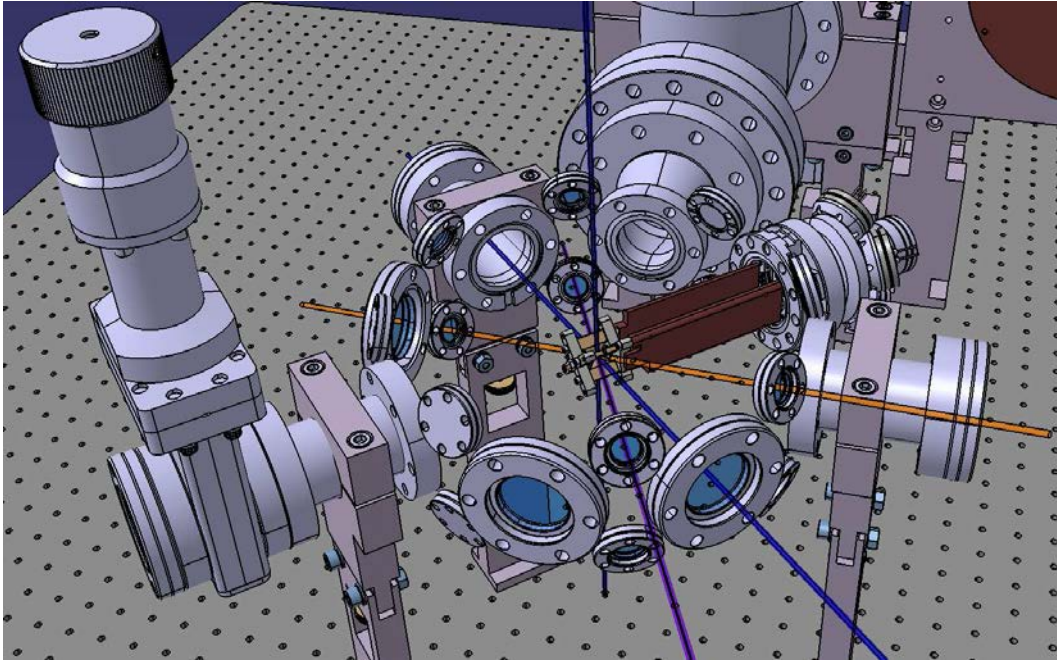
Figure 4.1: CAD drawing of the experiment chamber and the ion trap, where the chamber itself as well as the CF160 viewports on top and on bottom of it are hidden. Possible axes for the laser beams are indicated by blue (398.8 nm, ionization), purple (369.5 nm, ionization and cooling) and orange (935.2 nm, repump) rays.

itself has so called "grabber grooves" at each of the CF160 and CF40 ports[3] the ion trap could be connected directly to the experiment chamber. In such a design, each removal of the trap would inevitably require to remove at least one of the CF160 viewports. The solution was to connect the ion trap to a flange adapter[4] - which adds the grabber grooves to standard CF vacuum components - using two groove grabbers [5]. This flange adapter is finally connected to the vacuum chamber and to a multi-port flange[6] via CF40 sealing surfaces. The multi-port flange has five CF16 sealing surfaces of which four are used for electrical feedthroughs and one for optical access.

4.1.3 Pumps, Gauges and Valves

In order to achieve UHV conditions with a pressure of 1×10^{-10} mbar or below, it is necessary to work with a combination of different vacuum pumps. Here,

---

[3]These grabber grooves are visible in a section view of the vacuum chamber found in figure 5.9.

[4]Kimball Physics MCF275FlgAdprt-C2

[5]Kimball Physics MCF275GrvGrb-C01

[6]MDC Vacuum 409004

the following pumps have been used:

- a scroll pump producing a pressure below 0.1 mbar that is necessary for the turbo pump to work (Varian SH-110 Dry Scroll Vacuum Pump)

- a turbo pump with a pumping speed of $80 \, \mathrm{L \, s^{-1}}$, producing a pressure below $1 \times 10^{-9} \, \mathrm{mbar}$ (Pfeiffer Vacuum HighPace 80)

- an ion pump with a pumping speed of $100 \, \mathrm{L \, s^{-1}}$ (Gamma Vacuum 100L-DI-6D-SC-N-N)

- a titanium sublimation pump (Varian Mini T-Ball) mounted in a large CF100 tee next to the experiment chamber

- a Ti-Zr-V non-evaporable getter (NEG) coating on the entire inner surface of the experiment chamber (coating generously done by GSI Darmstadt)

The scroll pump and the turbo pump are used only until the end of the bakeout and leak searching procedure described in subsection 4.2.1. As the gas load in this kind of experiments is typically low, ion pumps and getter pumps are sufficient for maintaining a low pressure. Besides the NEG coating, all pumps have been bought before the start of the design process. The challenge now was to have the chamber efficiently pumped with the available pumps. For this purpose, all pipes between the pumps and the experiment should be wide and short: In the molecular gas regime, where collisions between gas particles are very rare, the pipe conductivity is

$$L_{pipe,molecular} = \frac{\bar{c}\pi d^3}{12l} \tag{4.1}$$

where d is the diameter of the pipe, l its length and $\bar{c}$ the mean thermal velocity of the gas.

As it was compulsory to use the CF160 sealing surfaces of the experiment chamber for high resolution imaging of the ions[7], the only reasonable way of pumping the chamber was to use a CF40 port. The inner diameter is 38 mm and the minimum length of a standard CF40 straight connector is about 80 mm. In an UHV system that has not been baked extensively, water is a common residual gas. For $m = 18u$ and $T = 300 \, \mathrm{K}$ one obtains $\bar{c} = 645 \, \mathrm{m \, s^{-1}}$ and $L = 116 \, \mathrm{L \, s^{-1}}$. As the goal was to use a sublimation pump in combination with an ion pump, which alone has a pumping rate of $100 \, \mathrm{L \, s^{-1}}$, the pipe conductivity of a straight CF40 connector is insufficient for exploiting the full pumping rate.

---

[7]The trap is nearer to a CF160 viewport than to a CF40 viewport, allowing for larger numerical aperture and consequently higher resolution.

In order to increase the pumping rate, we decided to use a conical CF63-CF40 reducer[8] for the connection of the chamber to the pumping system. Integration over L^{-1} yields for the conductivity of the conical reducer

$$L_{conical,molecular} = \frac{\bar{c}\pi \left(d_{63} - d_{40}\right) d_{63}^2 d_{40}^2}{6l \left(d_{63}^2 - d_{40}^2\right)}$$

where $d_{40} = 38\,\text{mm}$ and $d_{63} = 63\,\text{mm}$ are the diameters of a CF40 and a CF63 flange. $l = 75\,\text{mm}$ is the approximate length of the reducer. Its conductivity is accordingly $L_{conical,molecular} = 255\,\text{L}\,\text{s}^{-1}$.

The conical reducer is connected to a CF100 tee via a CF100-CF63 reducer flange. This CF100 tee itself is a vacuum pump, because a significant fraction of its inner surface can be coated with a titanium layer. Titanium is a very reactive chemical element - everyone who owns a wristwatch with titanium housing knows it immediately oxidizes - and therefore absorbs residual gases. Coating the tee with titanium is done using an electrically heated titanium sublimation source after bakeout. Detailed description of this procedure that might be repeated from to time to time depending on the residual gas load can be found in subsection 4.2.1. The titanium sublimation source is mounted to one of its flanges using a CF100-CF40 cluster flange[9] providing three CF40 flanges. Important aspects considering the position and orientation of the sublimation source were

- to have the titanium-coated surface inside the tee maximized.

- to ensure that neither the experiment nor the UHV gauge get coated with titanium.

In order to account for these, a custom made CF40 straight connector with total length $l = 76\,\text{mm}$ is put in between the cluster flange and the sublimation source. The same custom made parts are used for mounting the experiment chamber on the optical table.

The UHV gauge[10] is mounted to one of the CF40 flanges of the cluster flange, thus directly neighboring the titanium sublimation source. In order to avoid coating it with titanium during sublimation, the gauge had to be located inside a standard $l = 100\,\text{mm}$ CF40 straight connector. In principle, locating a vacuum gauge near the walls of the chamber is not ideal. The pressure might be overestimated, but here it seemed to be the most reasonable solution. Generally, locating the vacuum gauge at a position near the experiment is desirable. Yet, this would have inevitably led to a reduction of optical access.

The third flange of the tee is directly connected to one of the CF100 flanges of the ion pump. Via a CF100-CF40 reducer flange, a CF40 cross is connected

---

[8]MDC Vacuum 402032
[9]Vacom 300370
[10]Varian UHV-24P Ion Gauge

to the other side of the ion pump. A viewport is connected to one end of the cross, providing optical access through the entire vacuum system to the experiment. This is also where an all metal valve[11] is attached sealing the UHV system after the desired pressure is reached.

4.1.4   Possible Extensions

As was previously mentioned, the design for the ion trap experiment was aimed to be compatible with ultracold gas experiments. After it had been concluded at the very beginning of the design process that having a MOT and an ion trap inside the existent experiment chamber is not feasible, it was decided to have the possibility of extending the vacuum system by putting an additional vacuum chamber neighboring to the ion trap chamber. In order to have this extension performed at a later stage of the experiment without having to vent the entire UHV system, a comparably cheap CF40 gate valve[12] has been attached to the experiment chamber. The valve is specified for a minimum pressure of 1×10^{-11} mbar and bakeable to 200°C. It is sealed using a viton[13] ring, which - concerning sealing - is not the best option for UHV systems at all. A metal ring sealed valve would be significantly better and more expensive. In order to compensate for this imperfection, the valve will be left opened and sealed with a viewport as long as the extension is not done. Before connecting an additional vacuum chamber, the gate valve would have to be closed and the viewport removed. Although a temporary rise of pressure inside the ion trap chamber during the extension cannot be excluded, it is quite certain that a renewed bakeout will not be necessary.

4.2   Assembly

All steps of vacuum assembly were performed beneath a laminar flowbox, in a laboratory with low air humidity of about 20%. Besides latex gloves, no protective equipment was worn during assembly. All vacuum components were new and cleaned for UHV application. Nonetheless, some components have been cleaned with high purity acetone when the cleanliness was in doubt. To ensure the tightness of the CF seals, all knife edges of the sealing surfaces as well as the copper gaskets have been visually inspected directly before assembly. To be sure that sealing surfaces are free from larger dirt particles such as human hair they have been cleaned with a dusting gas only a few moments before pressing the flanges together. Of course, care was taken to tighten the flanges uniformly. Most of the flanges have been tightened until the distance

---

[11]VAT All Metal Angle Valve CF40 "easy close"

[12]MDC Vacuum 302012

[13]Viton is a thermally and chemically durable synthetic rubber with low outgassing rate.

between the sealing surfaces was below 0.1 mm. This leaves the possibility of eliminating small leaks by compressing the copper seals a bit more. Flanges that are mechanically strained, especially the three mounting tubes of the experiment chamber and the conical reducer, have been tightened as far as possible. Annealed copper gaskets[14] have been used for all of the viewports in order to reduce the risk of damaging them. As described later, no major leaks occurred at none of the flanges.

The first step of the assembly of the vacuum system was adding viewports, CF40 tubes for mounting purposes and blank flanges to the experiment chamber. Previously, the chamber had been NEG coated by GSI in Darmstadt, requiring all CF40 and CF16 flanges to be sealed with blank flanges. During assembly, the CF160 have been added first, and afterwards only one of the blank flanges is removed at a time, minimizing the risk of contaminating the interior of the chamber. After the experiment chamber was fully equipped, it was mounted on three self-designed, height adjustable mounts. The design height of the center of the experiment chamber above the table is 280 mm. This leads to a distance between the outer surfaces of the lower CF160 viewport and the table of approximately 207 mm. In the actual setup, the exact height of the experiment is given by the fixed height of the ion pump.

In the second step, the pumping section of the vacuum chamber consisting of the tee and the ion pump was fully assembled . Afterwards, the experiment chamber and the pumping section had to be joined. Certainly, this last step was the most difficult. The heights of each of the three mounts of the experiment chamber had to be carefully adjusted and corrected during the tightening of the flange. Nonetheless, this work had been done in only two hours and despite all doubts, this last flange later proved to be tight.

A picture showing the entire vacuum setup explaining positions of the components is provided in figure 4.2.

4.2.1 Pumping and Baking

During the preparation of the vacuum setup and prior to the first ion trapping attempts, the vacuum system has been pumped and baked five times, until finally a pressure in the range of 1×10^{-11} mbar was reached after titanium sublimation. In all cases the experiment chamber has been baked at a temperature of 140°C and the pumping section at 160°C. Ramping times were typically 12 hours. The baking temperature was maintained for several days. These comparably low baking temperatures haven been chosen in order to avoid an activation of the NEG coating. An activation was to be avoided for economic reasons, as it was not clear how many times the vacuum system would have had to be opened or will be opened in the future. The pump-

---

[14]Annealing the defects caused by mechanical machining makes copper a lot softer.

Figure 4.2: Vacuum setup prior to inserting the ion trap.

ing efficiency of the NEG coating decreases inversely proportional with the number of activation cycles. Several different types of activation cycles have been reported for NEG coatings. At GSI, the coating is activated by heating to 250°C for 24 hours. In reference [5], where the properties of TiZrV NEG coatings are investigated, the activation temperature is reported to depend on the actual composition and the microscopic structure. Both depend on sputtering parameters like cathode diameter, sputtering rate and sputtering pressure. For example, they report a coating with a composition of 30% titanium, 20% zirconium and 50% vanadium is completely activated by heating to 180°C for 24 hours. The parameters for the coating present in the chamber used for this experiment are not known. Another interesting aspect mentioned in this publication is that the aging effect of the NEG coating caused by repeated activation-air-venting cycles may be compensate for by increasing the activation temperature. Only during the final bakeout of the chamber (with ion trap), the temperature of the experiment chamber was increased to 160°C for 48h. During this master thesis, it has not been investigated systematically, whether the getter coating got activated at any of these low bakeout temperatures. Considering the very low final pressure, it seems likely that at least in some regions of the chamber, the coating got activated.

In the following, the iterations of pumping and baking are described in order to explain why the process had to be undergone five times. Only in the last of these steps, the ion trap was installed inside the vacuum chamber.

1. The valve connecting the vacuum chamber with the turbo pump had unfortunately been closed prior to first pumping and the chamber was not pumped at all. Unfortunately, this was not discovered before beginning

the bakeout, so that the vacuum chamber was baked to approximately 150°C with air inside leading to overpressure.

2. After pumping the chamber, during the second bakeout attempt, a black-out happened while the chamber was hot. Consequently, it was cooled down fast and uncontrolled.

3. The third pumping and bakeout procedure, for which the pressure is plotted in figure 4.3, was successful. As the lowest observed pressure was only 2×10^{-9} mbar - one order of magnitude more than expected - a leak was assumed and searched for using a helium leak detector. It turned out that the leak was caused by a damaged glass-metal seal of one of the CF16 viewports. Most likely, this damage has been caused by the overpressure due to unevacuated heating or the uncontrolled cooling down after the blackout. The leak rate of the window was measured to be 1×10^{-7} mbarL/s. As the pump rate is about $100 \, \mathrm{L \, s^{-1}}$, this explains the observed pressure very well.

4. The damaged viewport was replaced and the chamber pumped and baked again, in order to test how good the vacuum would get without an ion trap present. As expected, a pressure of about 1×10^{-10} mbar was reached, compare figure 4.4. The titanium sublimation source was moderately operated leading to a further pressure decrease down to 5×10^{-11} mbar after a few hours. The UHV gauge was started and both filaments degassed multiply. The ion pump was started and the cleaning function operated once.[15] A few hours were spent unsuccessfully searching for further leaks.

5. After finally the ion trap had been added to the setup, the chamber was pumped again. As expected, severe outgassing of the ion trap was observed, causing the pressure to remain about one order of magnitude larger compared with the setup without ion trap during all times until the end of the bakeout procedure. With ion pump in operation the pressure could be reduced down to about 5×10^{-10} mbar. For sufficient titanium sublimation, the current of the sublimation source was slowly ramped up from $30 \, \mathrm{A}$ (where basically nothing happens) to its maximum rated current of $50 \, \mathrm{A}$ during 40 minutes, where it was kept for 15 minutes and finally ramped down in about 15 minutes. A few hours later, the pressure had dropped to 3×10^{-11} mbar. In another attempt of leak testing, no leaks could be localized.

---

[15]In normal operation, the ion pump works with a voltage of $7 \, \mathrm{kV}$. During "high pot" operation, the voltage is ramped up to $10 \, \mathrm{kV}$ for a few seconds.
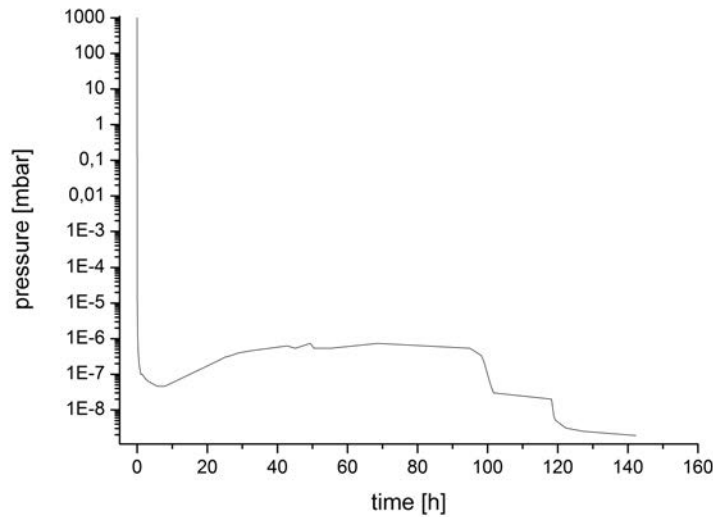
Figure 4.3: Pressure during pumping and bakeout, with a large leak present at one of the viewports. Measurement devices were the vacuum gauge delivered with the turbo pump (Pfeiffer Vacuum PKR 261, for pressures above 5×10^{-9} mbar) and the ion pump. The bakeout started two hours after the pumping began and reached its maximum temperatures of 140°C (experiment chamber) and 160°C (pumping section) 12 hours later. After three days of baking and the following ramp down of temperature, a pressure of 1×10^{-8} mbar was reached without ion pump. Activating the ion pump 118 hours after the pumping started, reduced the pressure to 2×10^{-9} mbar.
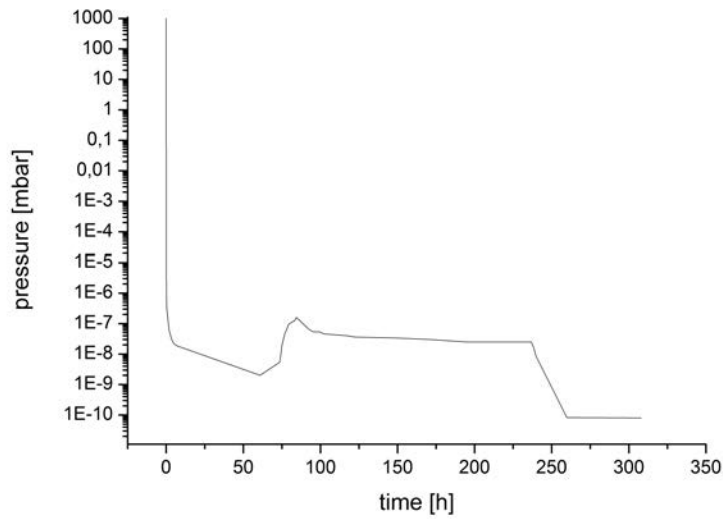
Figure 4.4: Pressure during pumping an bakeout for the chamber without ion trap and without leaks. Measurement as described above. Obviously the pressure before and after the bakeout is lower than in figure 4.3. Another important difference is the behavior of the pressure after the temperature reached it maximum value about 80 hours after the start of pumping: Here the pressure starts to fall again although the temperature remains high until about 240 hours.

Chapter 5

Optical System

Basically, the optical system used in this experiment consists of laser systems, optics for delivering the laser radiation to the ions and a microscope used for high resolution fluorescence imaging of the trapped ions. The latter could later be used for high precision illumination of ions at the fluorescence wavelength as well.

5.1 Laser Systems

This section gives a brief overview of the laser systems. They have been build and characterized within the context of the bachelor theses [28],[43],[65] and [69]. The lasers operating at the wavelengths 398.9 nm and 935.2 nm have been finished during these bachelor theses and are fully functional. Details about their performance as well as detailed technical information on stabilization techniques have been discussed in the bachelor theses extensively. During this master thesis it turned out that the laser system operating at 369.5 nm using an extremely cooled laser diode, kindly and very satisfactorily set up by Jascha Zander in his bachelor thesis [69], was not fit for long term operation. The problems with this laser system, which led us to design a new version optimized for diode cooling, are described in subsection 5.1.5. Besides this laser, all laser systems, as well as frequency stabilizations and beam deliveries to the experiment have been finished since January 2014. Detailed information about these systems will be found in the upcoming master thesis of Johannes Thielking.

5.1.1 Requirements

A level scheme for the ytterbium ion is shown in figure 5.1, the one for neutral ytterbium atoms had already been discussed in subsection 3.1.5. Natural linewidths of the ionization laser at 398.9 nm and the cooling laser at 369.5 nm

are 30 MHz and 20 MHz. Information on the natural linewidth of the repumping transition at 935.2 nm could not be obtained, but is expected to be in the range of some MHz as well. This repump laser has to be used, as the branching ratio for an ion in the state $^2P_{1/2}$ to decay to the metastable state $^2D_{3/2}$ is 0.48%. This means that without repump laser, the ion gets optically lost after about 200 cooling photons have been scattered. Calculations on this branching ratio have been published in reference [40] and experimentally verified according to reference [68]. With very low probability, the ion gets into the dark state $^2F_{1/2}$. As this state can only decay to the ground state via an octupole transition, it has - according to reference [31] - a lifetime of 6 years. In reference [50], the $^2F_{1/2}$ state is said to be populated only a few times per hour due to scattering with background gas. Thus, observing a trapped ion for hours or even days, would require a second repump laser at 638.6 nm. For economic reasons, this experiment is not equipped with this repump laser.
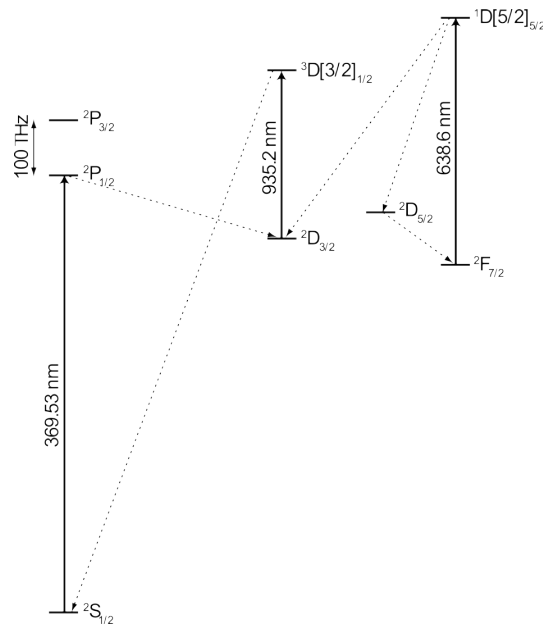
Figure 5.1: Lowest levels of the ytterbium ion. Taken from [50]. Doppler cooling and ion fluorescence are done using the transition at 369.5 nm. For infinite cooling, two repump lasers would be necessary. In this experiment, only the repump laser running at 935.2 nm is used.

Efficient Doppler cooling requires the laser linewidth to be significantly smaller than the natural linewidth of the cooling transition. Having a laser linewidth of 1 MHz would be fine for the beginning and should be easily achievable. Additionally, the cooling laser has to be tunable about a range of several 100 MHz, as the laser detuning is reduced during Doppler cooling. One typically starts with a red detuning of 20Γ and reduces it with tuning rates of $100 \, \text{MHz s}^{-1}$ to the value $\Gamma/2$, where the Doppler cooling limit is reached.

Cooling and repump lasers should saturate their transitions. In reference [30], where laser cooling of ytterbium ions using a setup very similar to the one here is described, necessary laser powers of $340\,\mu$W for the cooling laser and $4\,$mW for the repump laser are denominated.

For facilitating experimental procedures, long term frequency stability of all laser system should be as high as possible.

5.1.2 External Cavity Diode Lasers

An extensive treatment on the technique of optically stabilizing diode lasers using feedback from a diffraction grating can be found in [53], as well as in the bachelor theses mentioned at the beginning of this section.

Whenever a laser diode emitting at the required wavelength is available and the necessary optical power is not too high, using a laser diode based laser system is a good idea, as they are comparably cheap, compact and tunable. Besides poor beam profile, there is only one fundamental problem with laser diodes: Without using external feedback, the emission lines are tens of MHz wide, making them impossible to use out of the box in quantum optics experiments, where the laser in many cases has to address atomic transitions with very high precision. Laser diodes having such a larger linewidth can easily be understood from first principles:

- Laser transitions in diode lasers take place between valence band and conduction band in the band structure of a semiconducting material. Thus, the transition does not define the energy of a laser photon sharply. As a consequence, the gain curve of diode lasers is wide.

- The length of the laser resonator of a free-running laser diode is small, e.g. only several $100\,\mu$m. A short optical resonator has a comparatively large linewidth: Decreasing the length of an optical resonator for fixed mirror reflectivity causes the photons to be reflected from the mirrors more frequently, thus decreasing the lifetime inside the resonator. According to the uncertainty principle, physical systems with shorter lifetime have a less sharply defined energy. A quantitative treatment of this behavior can be found in reference [62].

An external cavity diode laser basically consists of a laser diode, an aspheric lens as collimation and a reflective diffraction grating. This is visualized in figure 5.2. The diffraction grating is adjusted in such a way that the first order of diffraction goes back into the laser diode, providing optical feedback. Hence, the diffraction grating forms, together with the rear side of the laser diode, an "external" resonator with the following properties:

- It is about $2\,$cm long, significantly longer than the internal resonator, thus

- its linewidth is far smaller.
- its free spectral range $\Delta\nu_{FSR} = \frac{c}{2L}$ is smaller, meaning the resonator modes are closer in frequency space.

- Its losses are adjustable, due to the wavelength selectivity of the diffraction grating.
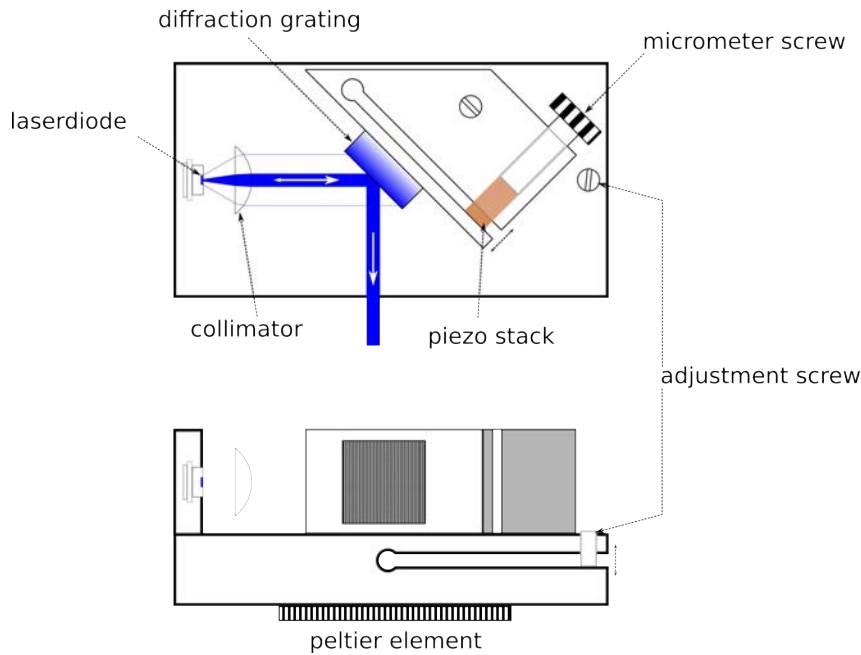
Figure 5.2: Schematic view of our external cavity diode laser design. Emerging from the laser diode, light is collimated using an aspheric lens. Afterwards it hits a reflective diffraction grating. The grating diffracts a small fraction of the light back into the laser diode. Two flexure bearings are used for alignment and tuning purposes. Rough tuning is done by hand with a micrometer screw, fine tuning and frequency stabilization with a piezo. For temperature stabilization the entire setup including external resonator is cooled by a PID controlled Peltier element. Taken from [65] with language adoptions.

The impact of these two effects and how they are used for reducing laser linewidth and increasing tunability is shown in figure 5.3: In an ECDL configuration, the laser is lasing in the external resonator mode which combines high gain of the laser medium with low loss of the external resonator. Tuning the laser can be done by tilting the diffraction grating, which has two effects:

- The length of the external resonator changes slightly, leading to a small change of the free spectral range and thereby shifts the modes. This is visualized by the green arrows.

- The wavelength of light which is preferably being diffracted back into the laser diode changes. This is equivalent to a change in the loss of the external resonator and visualized by the purple arrows.

Typically, using an external cavity reduces the linewidth of a diode laser to 100 kHz and provides mode-hop free tunability over a range of 6 GHz.
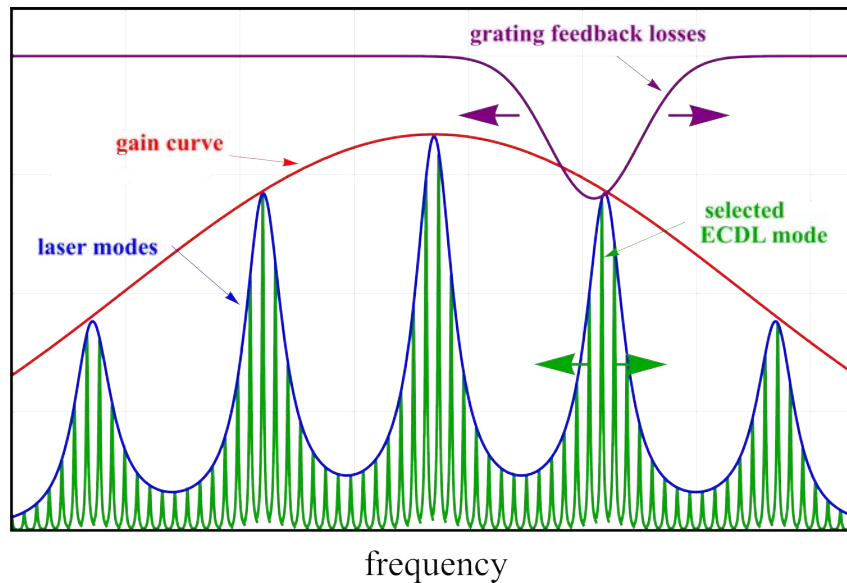
Figure 5.3: Visualization of the ECDL principle in frequency space. The ECDL modes are far narrower and closer than the modes of the free running laser diode. Their position is tunable. Taken from [29] with language adoptions.

By applying more sophisticated frequency stabilization techniques, where the laser is tuned actively using electronics, the laser linewidth can be reduced down to 1 Hz.

An important fact about laser diodes is their spectral dependence on temperature. For example, the central linewidths of the blue laser diodes used in this experiment change with $0.05\,\mathrm{nm\,K^{-1}}$. Thus, narrow, stable emission lines also require the laser to be temperature stabilized. Of course, this effect is also utilized for wavelength tuning. Our special design for operating an ECDL at temperatures well below 0°C, described in detail in 5.1.5, is a good example of this.

5.1.3   Frequency Stabilization

A further reduction of laser linewidth and increased long term stability of the emitted wavelength can be achieved by electronically locking the laser to a reference element, such as a vapor cell, an electronic wavelength meter or an

optical cavity. In the following, the principle of locking a laser to such a reference is briefly described for an optical cavity as reference. The construction of the narrow linewidth, high stability optical cavity used in this experiment as well as the locking technique have been extensively described in my bachelor thesis [65].

In the simplest case, an optical cavity consists of two mirrors with given distance and curvature. If certain criteria of stability are fulfilled, photons can get trapped between the mirrors, in the sense that they could in principle be reflected from one mirror to the other infinitely often, if no loss effects at the mirrors would occur. For simplicity, we consider a plane-parallel optical resonator. Such a resonator is on the edge of the stable parameter space, but becomes stable due to experimental imperfections. A perfect plane-parallel resonator is only characterized by its length L and the reflectivity $\mathcal{R}$ of the mirrors. It is "on resonance", if the wavelength λ of the incident light beam fulfills the standing wave condition

$$L = n\frac{\lambda}{2}, \ n\epsilon\mathbb{N}$$

For light with a wavelength on one of the resonances, the optical resonator is transparent. The distance in frequency for two such resonances defines the free spectral range of the cavity

$$\Delta\nu_{FSR} = \frac{c}{2L}$$

The width of each of these resonance is defined by the finesse

$$\mathcal{F} = \frac{\Delta\nu_{FSR}}{\Delta\nu}$$

where $\Delta\nu$ is the FWHM of transmitted power. If no loss processes inside the resonator are present and the reflectivities of the mirrors are exactly the same, the finesse is approximately given by

$$\mathcal{F} = \frac{\pi}{1 - \mathcal{R}}$$

A very powerful technique of locking a laser to narrow-linewidth spectral features, such as the resonances of an optical cavity or absorption due to atomic transitions, is frequency modulation spectroscopy, sometimes called RF spectroscopy. General aspects of this technique have been treated in reference [8]. If the reference element is an optical cavity, the technique is called Pound-Drever-Hall lock (PDH). An easily readable introduction to PDH is provided in reference [9].

The idea behind the PDH-lock is to shine laser light on an optical cavity, measure the amount of reflected light and tune the laser to resonance such

that this reflected light is kept at a minimum. In order to make this possible, the laser linewidth has to be slightly modulated. Otherwise it would not be possible for the locking electronics to know whether the laser frequency is larger or smaller than the reference frequency. By mixing the reflected signal with the modulation frequency and afterwards applying a low-pass filter, the reflection signal is transformed into a so called error signal, which has several zero-crossings. The laser is kept in resonance with the cavity by tuning it in such a way that the error signal is kept at zero.

5.1.4 Wavelength References

In the following, details on possible frequency references are summarized. Every of these references has the advantage compared to optical cavities that they allow for absolute frequency measurement.

5.1.4.1 Wavelength Meters

An easy but expensive method of measuring a lasers wavelength is to buy a commercial wavelength meter. These devices are available with absolute accuracies down to 2 MHz and measurement resolutions of 0.5 MHz. Their principle of operation is to record the interferometric patterns produced by Fizeau interferometers using CCD arrays. Data acquisition is possible with a repetition rate of up to 600 Hz. Using such a wavelength meter, it is possible to lock a laser to any wavelength. The best wavelength meter available to our group[1] has an absolute accuracy of 600 MHz and a resolution of 100 MHz. This wavelength meter is helpful for approximately tuning the laser to the resonant wavelength of an atom. But having a better wavelength meter use in our experiment would indeed be desirable.

Nils Roth investigated during his bachelor thesis, how a very simple and cheap wavelength meter can be build. It is based on a Michelson interferometer and works with a helium-neon laser as frequency reference. These lasers operate at a very well-known wavelength due to the laser medium having a bandwidth of only 0.002 nm. The wavelength meter worked at the end of the bachelor thesis and could measure wavelengths with an absolute accuracy of 300 MHz. Unfortunately, it was not brought that far that it could be used in automatic operation.

The principle of operation is explained here in a few words, for giving a beautiful example of wavelength measurement. Details on technique and results have been reported in Nils Roth's thesis [55].

A Michelson interferometer divides a light beam, lets both beams travel different distances and finally brings them to interference. Depending on the

----

[1] HighFinesse WS/6 High Precision

difference in length of the traveled path called g, there exists a certain phase ϕ between the light beams. This phase is given by

$$\phi = 2\pi \frac{g}{\lambda}$$

When bringing the beams to interference, for example on a photodiode, the observed intensity depends on this phase:

$$I(\phi) = \frac{I_0}{2}(1 + \cos(\phi))$$

The observed intensity is periodic in ϕ respectively g. Accordingly, one could in principle measure the wavelength λ by varying the path difference g by an exactly known length while counting the numbers of periods in $I(\phi)$ observed during this change. Another way, the way N. Roth did it, was to use the same Michelson interferometer with two laser beams at the same time - a reference beam produced by the helium-neon laser and the beam whose wavelength is to be measured. Two photodiodes are used for measuring the interference signals $I_{1,2}(g)$ of these lasers, depending on the path difference which is the same for both. The path difference is varied and the number of periods in the interference signal is counted for both lasers. The count starts and ends if minima in the interference patterns coincide. From the numbers of counted periods for the reference laser N_R, of the unknown laser N_U and the wavelength of the reference laser λ_R, the unknown wavelength is calculated to be

$$\lambda_U = \lambda_R \frac{N_R}{N_U}$$

The optical setup used for this wavelength measurement technique is sketched in figure 5.4.

5.1.4.2 Vapor Cells

The standard type of frequency reference, used whenever possible, is a vapor cell. They are typically build from vacuum components, are evacuated before use, contain a small amount of the specific chemical element and are heated to near the elements melting temperature. Viewports are used for performing absorption spectroscopy. As the linewidths are widened due to the Doppler effect, one has to apply saturated absorption spectroscopy. Vapor cells do not contain a noteworthy amount of ionized atoms and are therefore not usable as reference elements for ion experiments. In principle, one could have built a vapor cell as reference element for the 398.9 nm laser. For completeness, the following other aspects of using atomic references should be briefly mentioned:

Sometimes it is feasible to use a molecular instead of an atomic vapor cell, because molecules have very many spectroscopic features due to vibrational
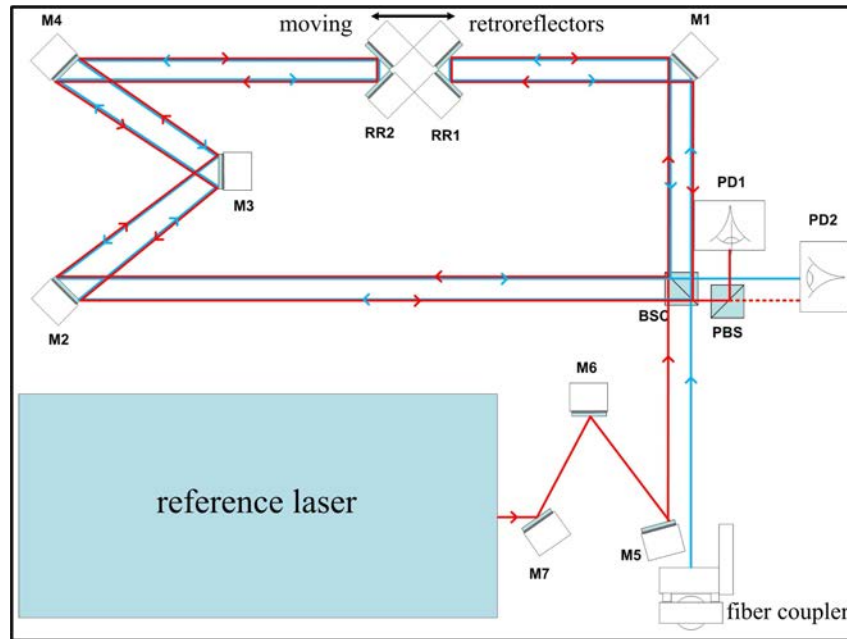
Figure 5.4: Sketch of the interferometer setup used as a wavelength meter. Basically, it consists of two Michelson interferometers. Taken from [55] with language adoptions.

and rotational states. Especially iodine offers many strong absorptions lines that could be used for locking purposes. Also to mention in this context are techniques such as cavity transfer locks, where an optical cavity is stabilized to an atomic reference and then serves as reference element for a second laser, and offset locking techniques. Currently, no plans to use such techniques in this experiment exist.

5.1.4.3 Galvatrons: DAVLL

Galvatrons, sometimes called hollow-cathode discharge lamps, produce a plasma of neutral and ionized atoms by a sputtering process: A large voltage is applied between an anode and a cathode located inside a chamber filled with a buffer gas. The cathode consists of the chemical element one is aiming for to perform spectroscopy on. Due to the high voltage, the buffer gas gets ionized, accelerated towards the cathode and sputters some of the material. Whether or to what extend ionized cathode material is present in the resulting plasma crucially depends on the composition of the buffer gas. The plasma can be used for laser locking with different types of absorption spectroscopy, one of them being dichroic atomic vapor laser lock (DAVLL). Thus, the problem of finding an atomic reference for ionized ytterbium can be solved by buying a galvatron containing ytterbium and the correct buffer gas. Here, the DAVLL technique as well as the experimental setup is briefly described following the

work done by D. Kielpinski presented in reference [61]. Due to the cooling problems with the 369.5 nm diode laser, no results on the application of this technique can be presented here. Most likely, they will be part of J. Thielkings upcoming master thesis[2].

Using galvatrons for spectroscopy of ions suffers from two major problems:

- Due to high pressure and temperature, the widths of absorption lines are increased to several GHz. For setups similar to ours, 3 GHz have been reported.

- Low ion density renders absorption comparably weak.

Both these problems are solved by the DAVLL technique, which is a form of Zeeman spectroscopy. The optical setup used for the galvatron are shown in figure 5.5. Using a static magnetic field of about 100 mG parallel to the laser direction, the two Zeeman components - right and left circularly polarized - of the relevant transition are split up. The linear polarizer (LP) located directly before the galvatron (HCL) ensures that both circular components are equally strong. Producing the magnetic field is done using strong neodymium magnets not shown in the figure. In the absorption spectrum of the galvatron[3], this results in two broad absorption lines. Passing the light through a quarter-wave plate (QWP), changes the basis in which the light is described and causes the polarizing beamsplitter (PBS) to split the light into the circular components. The intensity of both components is measured and subtracted in order to produce an error signal. This error signal has a zero-passing that can be used for laser locking.

5.1.5 Cooled ECDL

The laser diode used for providing light for cooling and fluorescence of the ion is a wavelength selected Nichia NDU1113E , running - at room temperature - at a central wavelength of about 371 nm. Accordingly, operating such a laser diode at a wavelength of 369.5 nm requires cooling to a temperature around -10°C.

During his bachelor thesis, Jascha Zander discovered that one of the four laser diodes bought emits light at a central wavelength of only 370.5 nm for low laser currents and later succeed in tuning this diode to the required wavelength in an ECDL setup by cooling to a temperature of 5°C. Unfortunately, this laser diode got destroyed by a high peak voltage occurring when one of

---

[2]In April 2014, J. Thielking successfully used the galvatron setup with the 398.9 nm laser. The linewidth of the galvatron absorption was measured to be about 2 GHz. For this spectroscopy on neutral ytterbium, strong absorption was observed and the galvatron's current had to be reduced in order to work with a lower atom density.

[3]H2783-70NE-Yb
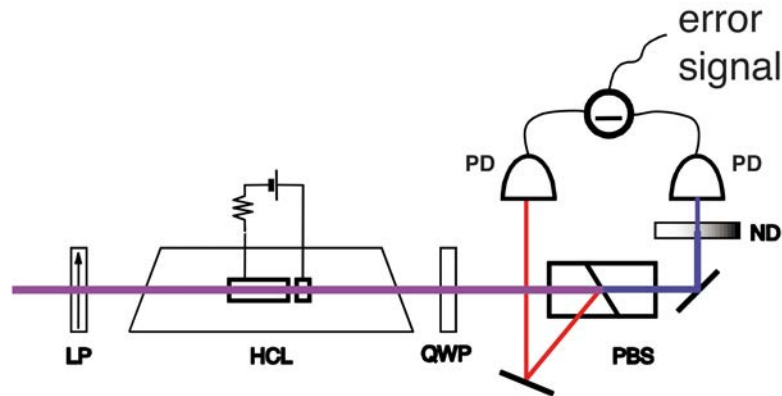
Figure 5.5: Visualization of the galvatron setup. The magnets necessary for the strong longitudinal magnetic field inside the galvatron are not shown. Taken from [61].

the laser's electric connections was removed during operation unthoughtfully. Efforts when using another laser diode showed that

- our standard ECDL design is not fit for cooling the laser diode below 0°C permanently, as heat removal on the hot side of the Peltier element is too weak and Peltier elements are too inefficient to maintain a temperature difference above 40 K.

- condensation of water on the optical surfaces significantly reduces laser output power and beam quality after a few days, although the laser housing is sealed and air drying measures have been taken.

After several weeks of testing with a second Peltier cooling stage, improved air drying and better housing seals, it was decided to design and build a new ECDL optimized for cooling to temperatures well below 0°C. Considering thermal properties, our design has been adopted from the one described in reference [16]. This design is reported to be able of permanently cooling a laser diode to -40°C. The laser should

- be capable of long term cooling the laser diode to -20°C. This is the minimum supported temperature of our standard laser and TEC driver[4]. Any condensation problems should not occur on the timescale of several weeks.

- have the same external resonator geometry as our established design. Changes to optomechanical components affecting laser performance, especially adjustable parts, should be kept as small as possible.

---

[4]Thorlabs ITC102

- remain fully tunable during low temperature operation.

In order to meet these requirements, the following changes were made to our laser design:

- In order to account for the decreasing efficiency of Peltier elements for high temperature differences the number of Peltier stages was increased from one to three. Sizes and powers of the Peltier elements have been chosen such that each Peltier stage is capable of transporting at least the heat produced by previous stages to its reservoir. Additionally, their powers have been chosen larger than necessary, as a Peltier element's efficiency drops if operated near full rated power. The chosen Peltier elements have specifications very similar to the ones reported in reference [16] and are listed in table 5.1.

- Underneath the last Peltier stage, a large heatsink equipped with heat fins has been added. Possibly, heat removal from the heat sink will have to be increased using fans. These fans should not be attached directly to the laser, as their vibrations have been observed to make stable laser operation impossible.

- A first step for the purpose of coping with water condensation on the optical surfaces is to have only the laser diode itself cooled to low temperature. In the previous design, the entire optical setup consisting of diode, collimator and diffraction grating was cooled. Accordingly, the laser diode had to be decoupled mechanically from the rest of the laser. This step could easily reduce mechanical stability of the optical setup, especially due to the fact that connections across Peltier elements can only be done using plastic screws, in order to avoid thermal bridges. This is compensated for by adding high precision dowel pins (plastics as well as stainless steel) to the design, fitting into high precision bores. In figure 5.7, the three Peltier elements are drawn in blue color.

- All parts of the housing are equipped with rubber seals. Wall thicknesses have been chosen large (10 mm) to provide large sealing surfaces.

- The laser window has been chosen to be relatively large, for ensuring usability of the laser design for other wavelengths, diffraction gratings and hence other deflection angles. It is also equipped with a rubber seal.

- All electric feedthroughs are realized using water tight 9-pin D-Sub connectors.

- The laser housing is larger than necessary, to have a large fraction of the volume filled with desiccant.

- Rough horizontal adjustment of the laser grating, which was done using a hand driven micrometer screw in the previous design, is now being done using a piezo driven actuator. This renders a mechanical feedthrough redundant. Besides, sensitivity and reproducibility of laser tuning should be increased by this modification.

- CAD drawings of the new laser are shown in figures 5.6 and 5.7.
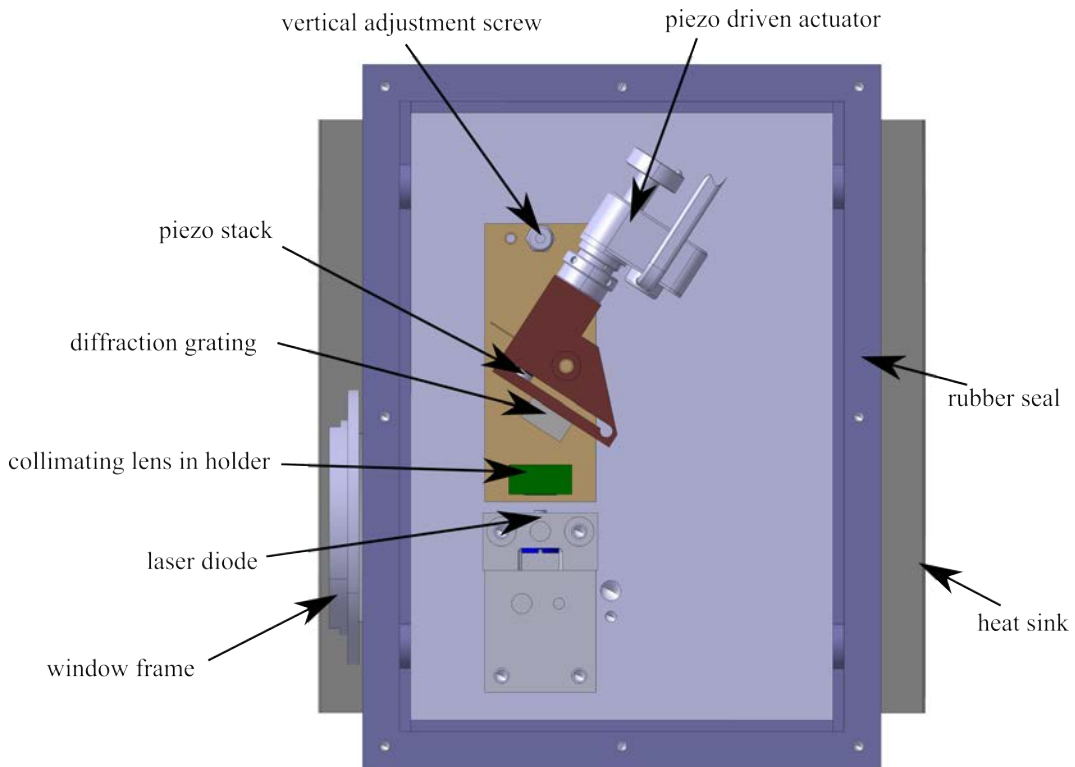
Figure 5.6: Cooled ECDL seen from above, with cover removed.

Peltier element	surface area [mm^2]	P$_{max}$[W]	U$_{typ}$[V]	I$_{max}$[A]
QC-17-1.4-8.5MS	15x15	9.5	2.1	8.5
QC-127-1.0-3.9M	30x30	34.5	15.5	3.9
QC-127-2.0-15.0M	50x50	110	15.5	15

Table 5.1: Specifications of the Peltier elements used in the new laser setup.

Alternatively, one could have tried to solve the water condensation problem by using an evacuated laser housing, as e.g. described by [14].
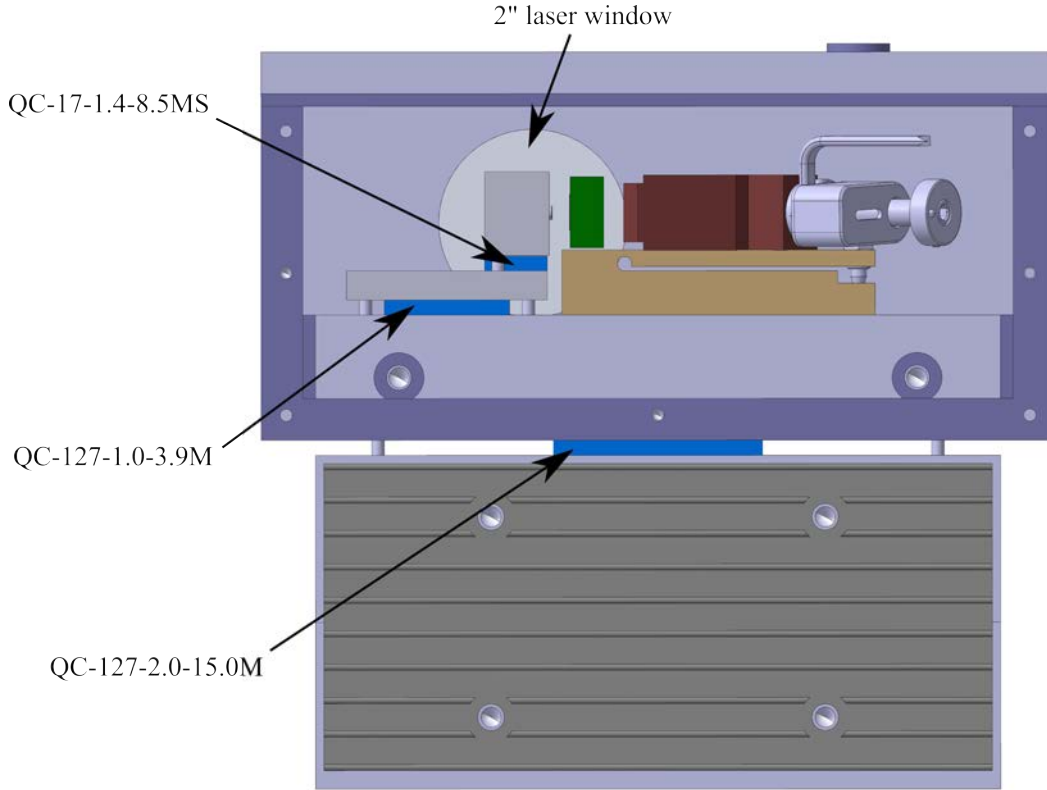
**Figure 5.7:** Cooled ECDL with one of housing walls being removed.

5.2 Microscope

The minimum requirements for the imaging optics are diffraction limited resolution, field of view of at least $100\,\mu m$ and adequate magnification for the single wavelength of $369.5\,nm$. With these specifications, the microscope is appropriate for imaging single ytterbium ions in an ion crystal. An optical imaging system is called diffraction limited if the spot size in its focal plane is about the same as the resolution given by the Rayleigh criterion where

$$Resolution = 1.22\frac{\lambda}{2NA} \tag{5.1}$$

NA denotes the numerical aperture defined below. According to reference [26] the imaging is diffraction limited if the peak-valley value of the deviation of the optical wavefront from a planar wavefront, the so called "wavefront aberration", is smaller than 0.25λ. Known from experience, this usually coincides with a RMS deviation of less than 0.07λ. Deviations of the wavefront are caused by the usual monochromatic optical aberrations such as spherical aberration, coma and astigmatism, and by imperfections of the surfaces of the optical elements.

The simplest microscope producing a real image consists of only two focusing lenses, as shown in figure 5.8. Light emerging from a point in the focal
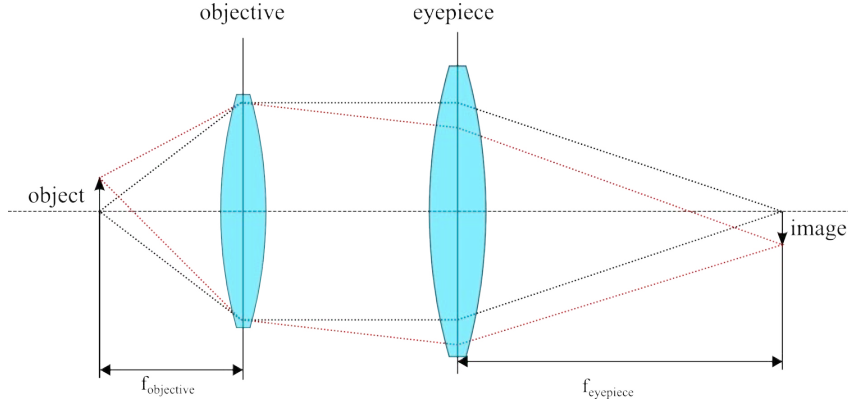
Figure 5.8: Simplest infinity-corrected microscope. Taken from [18] with language adaptions.

plane of the objective is collected and collimated before being refocused with another lens of different focal length. In this case, the magnification M of the microscope is simply given by the fraction of focal lengths

$$M = \frac{f_{eyepiece}}{f_{objective}} \tag{5.2}$$

5.2.1   Mechanical Boundary Conditions

Mainly, the mechanical restrictions of the microscope design are given by the distance d of the ion trap from the vacuum viewports and by their diameter D, defining the maximum numerical aperture

$$NA = \frac{D}{2d} \tag{5.3}$$

From the dimensions given in figure 5.9, the achievable numerical aperture is calculated to be 0.68, which would lead to an enormously high resolution of about 300 nm. Unfortunately, this would require very large and consequently expensive optics and would be very hard to adjust. Luckily, as the typical distance of ions trapped in a linear Paul trap is 5 μm, such a high resolution is not required and a numerical aperture of about 0.2 fully suffices for our purposes. As the distance from the ion trap to the CF40 viewports is about 120 mm and their view diameter is 35 mm, the numerical aperture of the imaging system would be limited to below 0.15 if a CF40 viewport was used. Such an imaging system would have a resolution of 1.6 μm. This would also be sufficient for imaging ions in an ion crystal. For convenience, we decided to use the large
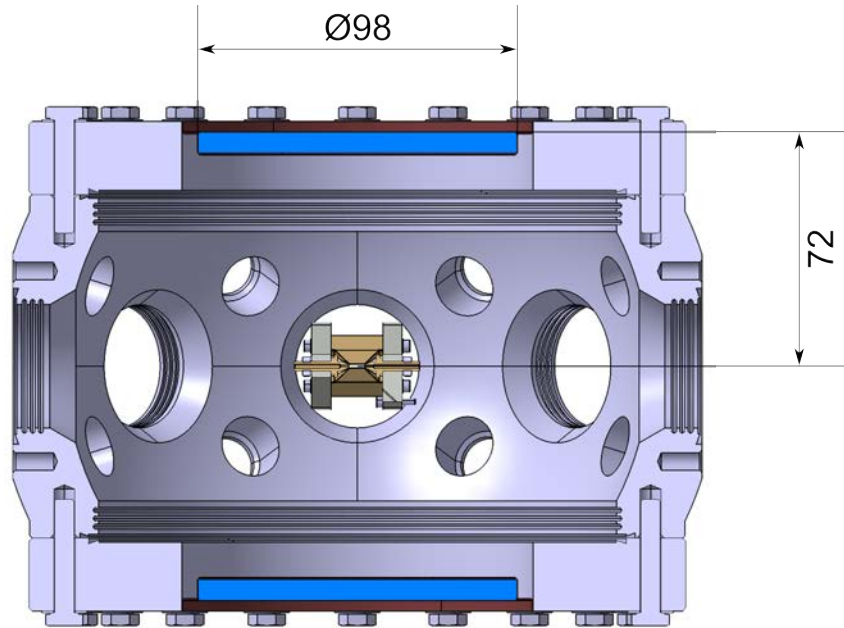
Figure 5.9: Section view of the experiment chamber with ion trap inside, unimportant features removed.

viewports and tried to find a low-cost solution of an imaging system with a resolution of 1 µm at least.

Considering the question which of the two CF160 viewports should be used for 370 nm imaging, it was decided to use the one at the bottom, as it does not require complicated mounting in large height above the optical table. The distance from the lowest surface of the bottom CF160 viewport to the optical table is 207 mm.

5.2.2 Optical Design

In the optical design process, the raytracing software OSLO Light Edition was used for minimizing wavefront distortion, maximizing the field of view and characterizations. During the entire process, the surfaces of the optical elements were assumed to be perfect, or at least good enough for diffraction limited imaging. The choice of optical elements for the imaging system was complicated by the necessity of finding elements made from glasses with acceptable coefficients of transmission in the UV.

I aimed for a preferably cheap microscope with as few optical elements as possible and fulfilling the specifications given in the introduction of this section. The microscope is required to have good imaging properties at a single wavelength, only. Hence, no dispersion effects had to be compensated and we assumed the specifications could be met using a setup consisting of only two

lenses. It was decided to build such a two lens infinity-corrected microscope as shown in figure 5.8. Of course, this cannot be done using spherical lenses only, as they produce large aberrations, making diffraction limited resolution impossible. Using spherical lenses only, such resolution requires a larger number of lenses which makes optical design as well as assembly significantly more difficult. Instead, it was decided to use an aspheric lens as objective lens, perfectly aberration compensated at the design wavelength. Considering imaging quality, the objective lens is decisive. Consequently, it has been selected at the beginning of the design process.

5.2.2.1 Choice of Aspheric Lens

In order to have a large numerical aperture, the diameter of the objective should be as large as possible. Besides, the focal length has to be larger than 72 mm. In principle, it would be feasible to locate the objective lens inside the vacuum chamber leading to higher numerical aperture, a smaller lens with shorter focal length and less surface imperfections. Due to the mechanical problems connected with this solutions, especially concerning adjustability, it was not taken into consideration seriously. The material should be fused silica or N-BK7, the design wavelength as close as possible to 370 nm and the quality of the surfaces not limiting the achievable resolution. In principle, one could have designed an aspheric lens optimized for our experiment and have it manufactured by the company Asphericon which produces custom made lenses and has a catalog of standard lenses as well. As it turned out, the price for a custom made lens is on the scale of 10k€, even if it is only a slightly modified version of a standard asphere. Luckily, the only available lens matching our requirements with respect to numerical aperture and material turned out - during OSLO simulations - to work fairly well at our wavelength. It is an uncoated fused silica asphere[5], designed for a wavelength of 285 nm, with a diameter of 50 mm and an effective focal length of 80 mm. A wavefront analysis for the lens can be found in figure 5.10.

5.2.2.2 Window Compensation

The second step in the optical design process was to find a way to compensate for the larger aberrations produced by the fused silica viewport with a thickness of 6.35 mm. This thickness was measured before beginning vacuum assembly using one of the CNC milling machines in our workshop. Compensation of the wavefront deformation visualized in figure 5.11 is inevitable, as these aberrations increase the resolution of the microscope to 160 µm making single ion imaging impossible. The strategy for compensating the effects caused by the window was to choose the eyepiece lens of the microscope accordingly.

---

[5]Asphericon 50-80 FPX-S-U
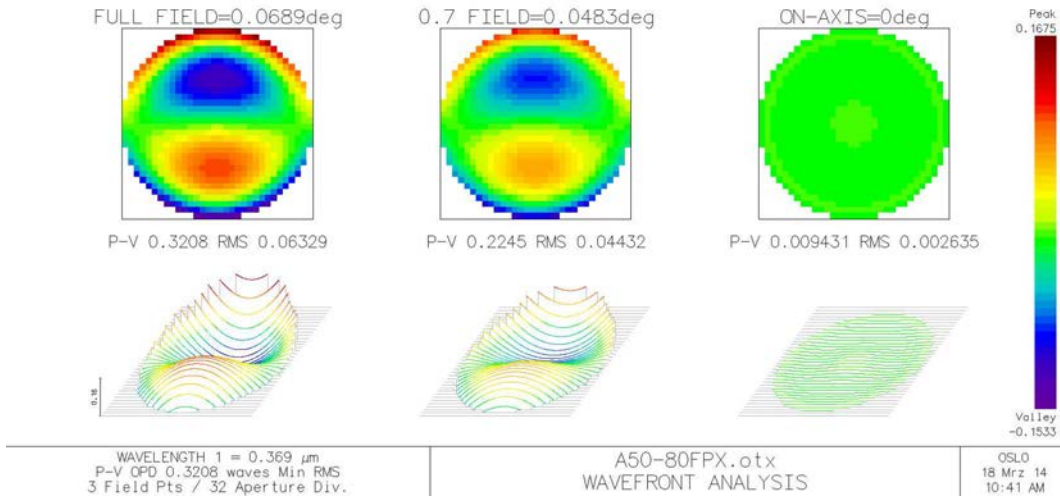
Figure 5.10: Wavefront analysis of the objective lens at 369 nm, for objects at different positions in the focal plane. The field of view is 100 µm, what means that the wavefront analysis on the very left, marked as "Full Field", has been performed with a point-like object being 100 µm away from the optical axis. For having (roughly) diffraction limited imaging, the numerical aperture had to be reduced to 0.2.

Basically, this was done by trying out several standard 2" singlet lenses and achromats from different optics manufacturers. During this process we found out that the wavefront aberration for imaging of objects not located on the optical axis strongly depends on the distance between the lenses. Consequently, this distance was also optimized.

Efforts using singlet lenses that would have been available with very high surfaces quality, were not successful, as these lenses themselves add aberrations. Finally an achromat distributed by Thorlabs[6], having a focal length of 500 mm, was found to compensate for the aberrations fairly well if placed at a distance of about 1 m from the asphere. With compensation the radius of the diffraction limited field of view of the imaging system even increased from about 100 µm in the case without window to 200 µm. Detailed information about the wavefront aberration and other optical properties of the imaging system finally build can be found in the following.

5.2.2.3 Characterizations

Without considering the surface qualities of the optical elements, the microscope should provide diffraction limited imaging of a field of view with a radius of 190 µm, compare figure 5.12. The magnification is approximately 6, a useful

---

[6]AC508-500-A
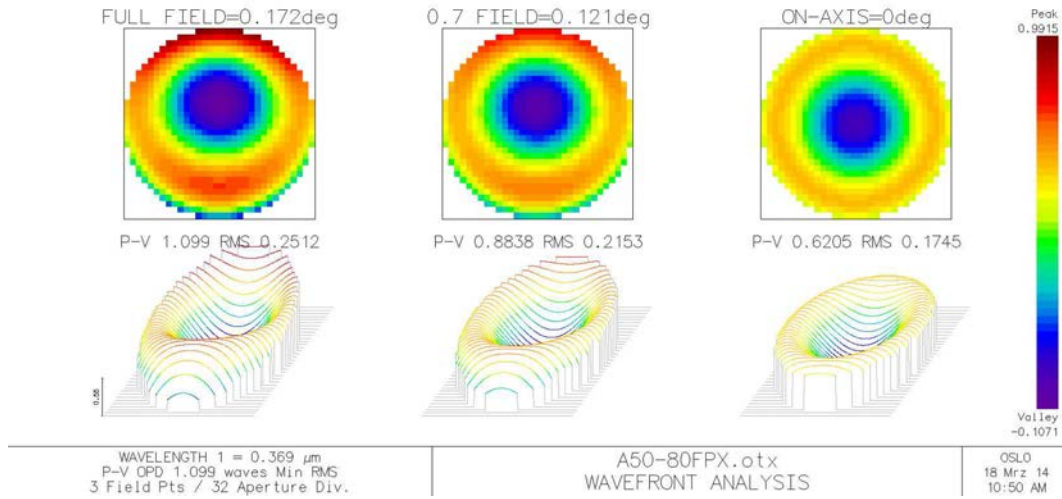
Figure 5.11: Wavefront analysis of the objective lens in combination with the window, prior to correcting wavefront aberration. Field of view: 100 µm. Numerical aperture: 0.2

value considering the pixel size of the camera[7] of 3.75 µm.

At later stages of the experiment, it might be useful to know the properties of this optical setup at wavelengths different from 369 nm. According to results from simulations performed with OSLO, listed in table 5.2, the system is also usable for diffraction limited imaging at longer wavelengths. Due to the small numerical aperture of 0.22 at maximum, the spot sizes are comparably large, nonetheless. Additionally, large focal shifts, measured with respect to the focal length at the ion fluorescence wavelength, occur. Hence, operating the microscope at multiple wavelengths at a time is not feasible. Still, it might be useful for adjusting purposes, e.g. prior to loading ions into an optical trap, produced with another similar microscope above the vacuum chamber.

An important question considering optical setups is their sensitivity towards imprecise adjustments, meaning translational- and tilting errors. The impact of such errors has been investigated, again using OSLO. One useful result is that the distances between objective lens and viewports, as well as the distance between the two lenses, is not important for imaging, as long as the latter is approximately 1 m. Table 5.3 lists the maximally tolerable adjustment errors, assuming diffraction limited imaging is at least required in a field of view with radius 100 µm.

---

[7]Point Grey CMLN-C3S2M-CS, equipped with CCD chip Sony ICX445, quantum efficiency approximately 35%@369 nm
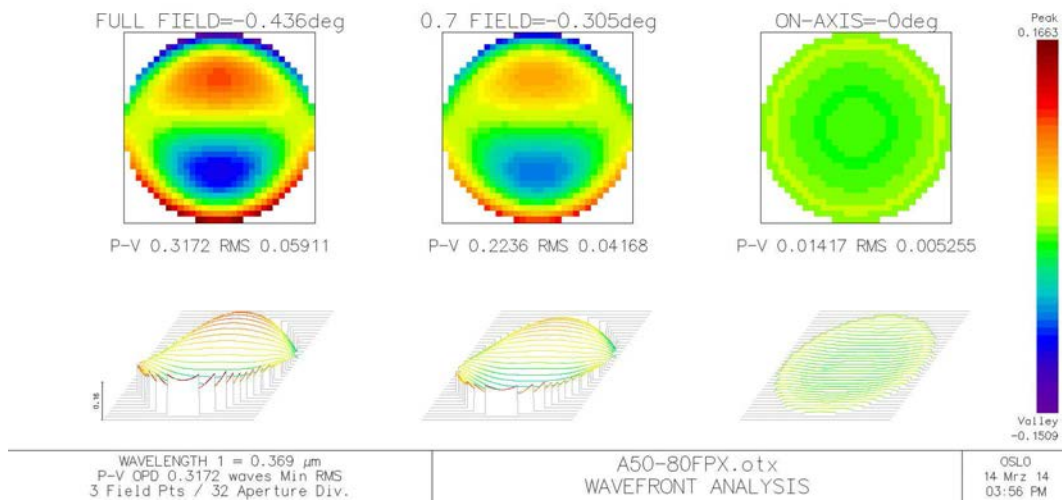
Figure 5.12: Wavefront analysis for the microscope setup, assuming a wavelength of 369 nm, for objects at different positions in the focal plane. The field of view is 250 µm. Imaging is diffraction limited up to a distance of 190 µm (not visible in this figure).

5.2.2.4 Surface Qualities

Until now, the surface quality of the optical elements had not been taken into account. The specifications of the optical surfaces are as follows:

- viewport: $\lambda/4$ - roughness, most likely peak-valley, λ probably 632 nm

- asphere: 300 nm rms wavefront deviation

- broadband mirrors: scratch-dig 20-10 for 2" and 10-5 for 1", typically corresponding to $\lambda/8$ respectively $\lambda/16$ peak-valley

- achromat: 40-20 scratch-dig, typically corresponding to $\lambda/4$ peak-valley

Obviously, the wavefront deviations of the asphere are limiting. From this data, it cannot be concluded to what extent the actual resolution of the microscope is going to be affected, as the distribution of the surfaces imperfections on the asphere is not known. It might well be that deviations occur primarily near the edge of the lens. As the microscope is going to be operated with reduced numerical aperture in any case, these deviations would not reduce imaging quality.

Of course, the low surface quality of the asphere is quite unsatisfactory. Spherical lenses are available with far smaller surface irregularities down to $\lambda/10$. Maybe, a similarly performing microscope could have been realized by an arrangement of spherical lenses. But the use of a single aspheric lens instead of a significantly higher number of spherical lenses also reduces the number of

λ[nm]	rms spot size x/y [µm]	rms spot size r [µm]	diffraction limit [µm]	focal shift [mm]
369	4.7×10^{-2}.	6.7×10^{-2}	1.0	0
399	3.8×10^{-2}	5.4×10^{-2}	1.1	+0.5
532	2.9×10^{-1}	4.0×10^{-1}	1.5	+2.2
780	6.2×10^{-1}	8.8×10^{-1}	2.2	+3.5
1064	9.0×10^{-1}	9.0×10^{-1}	2.9	+4.2

Table 5.2: Spot sizes and focal shifts for interesting wavelengths. Surprisingly, the microscope is diffraction limited for all of these wavelengths with sufficiently large field of view. Unfortunately, large focal shifts, measured with respect to the focal length at 369 nm, cause it not to be usable at multiple wavelengths simultaneously.

component	translation [mm]	tilt [°]
window	-	0.6
asphere	0.9	0.05
achromat	0.4	0.25

Table 5.3: Limits for maximally allowed adjustment errors, for diffraction limited imaging.

optical surfaces. Besides, using a single asphere is charming, as it dramatically reduces the mechanical degrees of freedom of the setup. Using an objective consisting of several spherical lenses would have required a very precise and stable mounting of the lenses relative to each other. This is hard to achieve without falling back on expensive commercial solutions. Another alternative, if the resolution should turn out to be too low, is to have a higher precision custom aspheric lens produced.

5.2.3   Mechanical Design

For simplicity, the optomechanics used for the objective are very similar to the ones used in the lithium experiment in our group, described in reference [18]. The setup is shown in figure 5.13. The movable parts consist of a xy-stage[8] providing translational adjustment with an accuracy of 1 µm and a self-designed tilting stage that is also used for translation along the z-axis. As this tilting stage uses three fine-thread screws with a winding pitch of 250 µm, height adjustments with an accuracy down to 10 µm should be achievable by simultaneously adjusting all three screws. The depth of field - meaning the maximum distance between object and focal plane of objective, for which the

---

[8]Owis KT 150-D80

imaging is still diffraction limited - of the objective is[9]:

$$DOF = 4\lambda \left(f\#\right)^2$$

The f-number $f\# = \frac{1}{2}NA$ is a quantity commonly used in photography instead of numerical aperture. It is defined simply as the ratio of focal length to the aperture of the first element. Here, the $f\#$ is approximately 2. So, the depth of field is

$$DOF \approx 6\,\mu m$$

Accordingly, the accuracy of the tilting stage is sufficient for focalizing the ions. The three bearing points of the tilting state are about 10 cm apart, leading to an accuracy for angle adjustments of about 0.005°, one order of magnitude better than necessary.

Both the translational as well as the tilting stage have a large aperture of 80 mm respectively 70 mm making it possible to use them for mounting an objective lens with a numerical aperture of about 0.45. This might be necessary at a later stage of the experiment. In the current setup, the aperture is limited by the diameter of two 2" $= 50.8$ mm mirrors[10] used under an angle of 45°, one of them shown in figure 5.13. Parts from the Thorlabs 2" cage system are used for mounting the asphere. Due to space restrictions, the asphere had to be glued to one of the cage plates.

The remaining parts of the imaging system - another two broadband mirrors and the achromat used as eyepiece lens - are mounted using highly stable, high accuracy, lockable mirror mounts[11]. For focusing the image on the camera, the eyepiece lens is additionally mounted on a linear stage[12]. The overall microscope setup can be seen in figure 5.14.
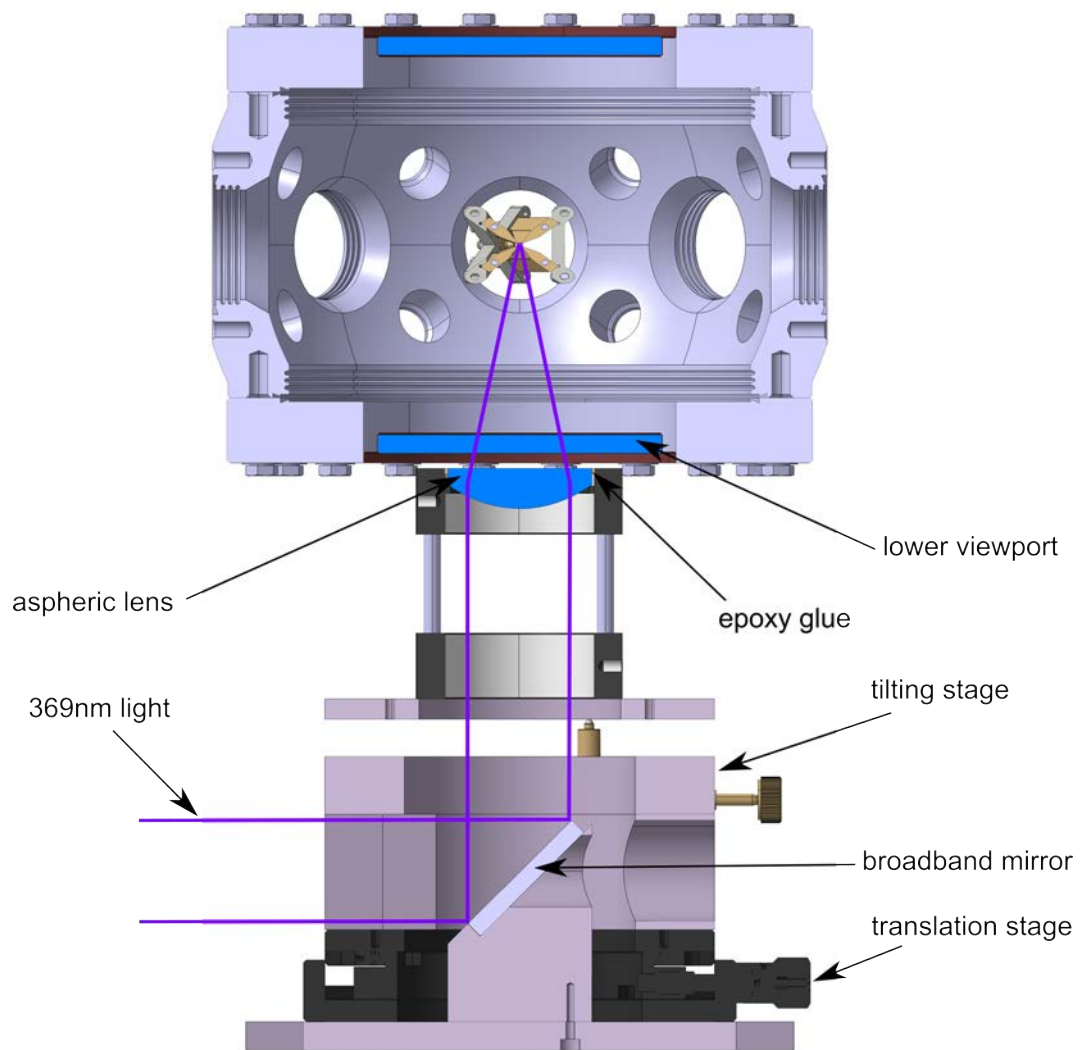
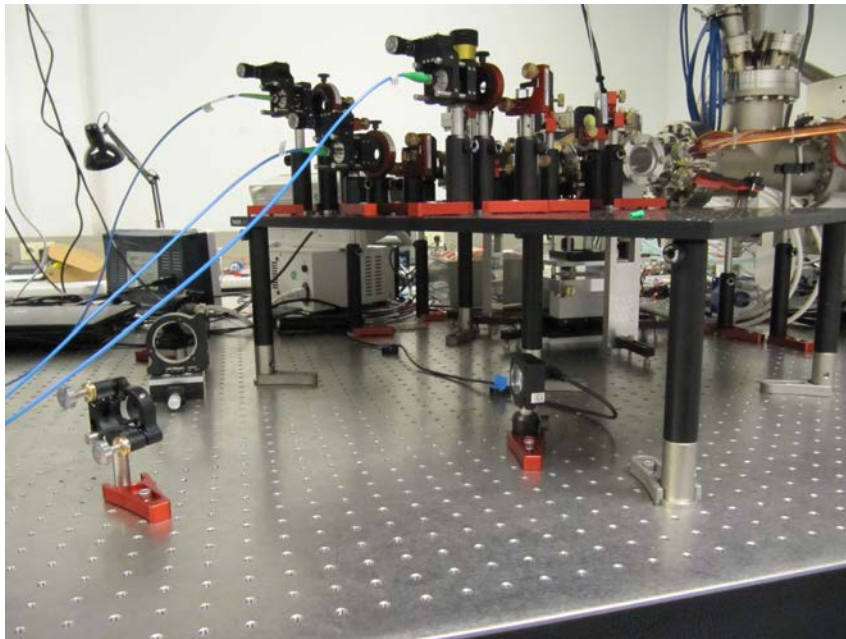---

[9]formula according to [18]

[10]Semrock MaxMirror MM2-311-50.8

[11]Newport U100-AC2K and U200-AC2K

[12]Thorlabs MT1/M

Figure 5.13: Section view of the microscope's objective.

Figure 5.14: Picture of the optical setup. Beam delivery for all three lasers is mostly situated on a breadboard. The laser beams are delivered from another optical table using optical fibers. Underneath the experiment chamber, the objective part of the microscope is visible. Light collected by the objective lens is guided to the camera using three broadband mirrors, two of them mounted in highly stable, lockable mirror holders. The eyepiece lens (on the left, covering one of the broadband mirrors) necessary for focusing the light onto the camera (located underneath the breadboard) is also mounted to a mirror holder and additionally to a translational stage.

Chapter 6

Conclusions and Outlook

In the course of this master thesis, a multi-purpose ion trap setup was designed and created. All necessary components except for the cooling laser are operational. To a large extend, they have been shown to meet specifications. Yet, we could not attempt to trap ions due to the missing cooling laser. Accordingly, proof that the setup as a whole will work is still pending.

The project started in April 2013 with the design of the ion trap, the vacuum system and RF drive electronics. The mechanical design was finished after three months. Assembly of the vacuum system started in August 2013. It was finished in about two weeks. Afterwards, the vacuum system was pumped and leak testing procedures applied. Meanwhile, the optical and mechanical design for the detection optics was finished. A sufficiently low pressure was obtained at the end of October 2013 after multiple iterations of pumping, baking and leak testing. In November 2013, the ion trap was assembled and added to the vacuum system. A renewed pumping of the chamber led to a pressure in the regime of ultra high vacuum without any problems. Also in October 2013, work started on finalizing the laser systems that had been built and characterized before in several bachelor theses. In December 2013 and January 2014, the RF system and the detection optics have been assembled. Around this time, the cooling laser was discovered not to meet our specifications concerning long term operation. Consequently, it was aimed at designing a new laser, capable of operating a laser diode at temperatures well below 0°C for many weeks without any water condensation problems. This laser should be assembled and ready for operation around the end of May 2014.

The next steps on the way to trap ytterbium ions include finishing the oven electronics and assembling the cooling laser. While this laser is not operational, one could try to observe fluorescence of neutral ytterbium atoms. This would prove ovens and the ionization laser work as required. Once fluorescence from trapped ions is observed, the loading process, ion cooling and external field compensation could be optimized. Many characterization measurements will have to be performed on the machine, e.g. to obtain the trapping frequencies.

Another important step will be the loading of specific low numbers of ions, e.g. one or two ions. When this is done, one could aim to realize single ion addressing with lasers and later to implement simple quantum algorithms. Alternatively, larger ion crystals could be created, cooled and their properties investigated. Cooling of ion crystals itself is challenging.

A further possible direction would be the purely optical trapping of ions, similar to experiments in the group of T. Schätz described in reference [20]. Possible schemes include trapping single ions in well localized dipole traps or trapping strings of ions in a one dimensional optical lattice. An example of experiments with ions in one-dimensional optical lattices can be found in reference [27]. Optically trapped ions could combine the benefits emerging from their strong Coulomb interaction with the almost arbitrarily selectable geometries and arrangements of optical traps. Of course, experiments with optically trapped ions would benefit from the absence of micromotion. However, they are challenging due to the comparatively weak trapping. Possible future experiments also include experiments where ions interact with ultra cold quantum gases or with Rydberg atoms. For such experiments, the entire setup including the vacuum system would have to be extended. Preparations for such an extensions have been made during this thesis and could be realized, as soon as the ion trap works and is well understood.

Bibliography

[1] R Alheit, K Enders, and G Werth. Isotope separation by nonlinear resonances in a Paul trap. *Applied Physics B*, 62(5):511–513, 1996.

[2] R Alheit, S Kleineidam, F Vedel, M Vedel, and G Werth. Higher order non-linear resonances in a Paul trap. *International Journal of Mass Spectrometry and Ion Processes*, 154(3):155–169, 1996.

[3] C. Balzer, A. Braun, T. Hannemann, C. Paape, M. Ettler, W. Neuhauser, and C. Wunderlich. Electrodynamically trapped Yb^+ ions for quantum information processing. *Physical Review A*, 73(4):041407, 2006.

[4] Ayan Banerjee, Umakant D Rapol, Dipankar Das, Anusha Krishna, and Vasant Natarajan. Precise measurements of UV atomic lines: Hyperfine structure and isotope shifts in the 398.8 nm line of Yb. *EPL (Europhysics Letters)*, 63(3):340, 2003.

[5] Cristoforo Benvenuti, P Chiggiato, P Costa Pinto, A Escudeiro Santana, T Hedley, A Mongelluzzo, V Ruzinov, and I Wevers. Vacuum properties of TiZrV non-evaporable getter films. *Vacuum*, 60(1):57–65, 2001.

[6] DJ Berkeland, JD Miller, JC Bergquist, WM Itano, and DJ Wineland. Minimization of ion micromotion in a Paul trap. *Journal of Applied Physics*, 83(10):5025–5033, 1998.

[7] Alberto Berton, Pietro Traldi, Li Ding, and Francesco L Brancia. Mapping the stability diagram of a digital ion trap (DIT) mass spectrometer varying the duty cycle of the trapping rectangular waveform. *Journal of the American Society for Mass Spectrometry*, 19(4):620–625, 2008.

[8] GC Bjorklund, MD Levenson, W Lenth, and C Ortiz. Frequency modulation (FM) spectroscopy. *Applied Physics B*, 32(3):145–152, 1983.

[9] E.D. Black. An introduction to Pound–Drever–Hall laser frequency stabilization. *American Journal of Physics*, 69:79, 2001.

[10] KR Brown, C Ospelkaus, Y Colombe, AC Wilson, D Leibfried, and DJ Wineland. Coupled quantized mechanical oscillators. *Nature*, 471(7337):196–199, 2011.

[11] Pavel Bushev, Daniel Rotter, Alex Wilson, François Dubin, Christoph Becher, Jürgen Eschner, Rainer Blatt, Viktor Steixner, Peter Rabl, and Peter Zoller. Feedback cooling of a single trapped ion. *arXiv preprint quant-ph/0509125*, 2005.

[12] Moses Chung, Erik P Gilson, Ronald C Davidson, Philip C Efthimion, and Richard Majeski. Use of a Linear Paul Trap to Study Random Noise-Induced Beam Degradation in High-Intensity Accelerators. *Physical Review Letters*, 102(14):145003, 2009.

[13] J Ignacio Cirac, R Blatt, AS Parkins, and Peter Zoller. Preparation of fock states by observation of quantum jumps in an ion trap. *Physical Review Letters*, 70:762–765, 1993.

[14] Eryn C Cook, Paul J Martin, Tobias L Brown-Heft, Jeffrey C Garman, and Daniel A Steck. High passive-stability diode-laser design for use in atomic-physics experiments. *Review of Scientific Instruments*, 83(4):043101, 2012.

[15] Ronald C Davidson, Hong Qin, and Gennady Shvets. A Paul trap configuration to simulate intense non-neutral beam propagation over large distances through a periodic focusing quadrupole magnetic field. *Physics of Plasmas*, 7(3):1020, 2000.

[16] Brian DeMarco. *Quantum behavior of an atomic Fermi gas*. PhD thesis, University of Colorado, 2001.

[17] RH Dicke. The effect of collisions upon the Doppler width of spectral lines. *Physical Review*, 89:472–473, 1953.

[18] Jan Henning Drewes. Aufbau eines hochauflösenden optischen Systems zur Untersuchung ultrakalter Quantengase, 2012.

[19] Michael Drewsen and Andy Brøner. Harmonic linear paul trap: Stability diagram and effective potentials. *Physical Review A*, 62(4):045401, 2000.

[20] Martin Enderlein. *Optical ion trapping for (scalable) quantum simulations and ultracold chemistry experiments*. PhD thesis, Universitätsbibliothek Freiburg, 2013.

[21] Jürgen Eschner, Giovanna Morigi, Ferdinand Schmidt-Kaler, Rainer Blatt, et al. Laser cooling of trapped ions. *JOSA B*, 20(5):1003–1015, 2003.

[22] Erik P Gilson, Moses Chung, Ronald C Davidson, Philip C Efthimion, Richard Majeski, and Edward A Startsev. Simulation of long-distance beam propagation in the Paul trap simulator experiment. *Nuclear Instruments and Methods in Physics Research Section A: Accelerators, Spectrometers, Detectors and Associated Equipment*, 544(1):171–178, 2005.

[23] Rudolf Grimm, Matthias Weidemüller, and Yurii B Ovchinnikov. Optical dipole traps for neutral atoms. *arXiv preprint physics/9902072*, 1999.

[24] Stephan Gulde. *Experimental realization of quantum gates and the deutsch-josza algorithm with trapped $^{40}Ca^+$–ions*. PhD thesis, 2003.

[25] Theodor W Hänsch and Arthur L Schawlow. Cooling of gases by laser radiation. *Optics Communications*, 13(1):68–69, 1975.

[26] E Hecht. Optik, 2009.

[27] Leon Karpa, Alexei Bylinskii, Dorian Gangloff, Marko Cetina, and Vladan Vuletić. Suppression of ion transport due to long-lived subwavelength localization by an optical lattice. *Physical Review Letters*, 111(16):163002, 2013.

[28] Andreas Kerkmann. Aufbau eines Diodenlasersystems bei 935nm für die Quanteninformationsverarbeitung, 2013.

[29] Hans Keßler. Aufbau eines blauen Lasersystems als Lichtquelle für eine Ytterbium 2D-MOT, 2011.

[30] D. Kielpinski, M. Cetina, JA Cox, and F.X. Kaertner. Laser cooling of trapped ytterbium ions with an ultraviolet diode laser. *Optics Letters*, 31(6):757–759, 2006.

[31] SA King, RM Godun, SA Webster, HS Margolis, LAM Johnson, K Szymaniec, PEG Baird, and P Gill. Absolute frequency measurement of the $^2S_{1/2}$–$^2F_{7/2}$ electric octupole transition in a single ion of ^{171}Yb$^+$ with 10^{-15} fractional uncertainty. *New Journal of Physics*, 14(1):013045, 2012.

[32] W Koczorowski, G Szawioła, A Walaszyk, A Buczek, D Stefańska, and E Stachowska. Experimental investigation of the stability diagram for Paul traps in the case of praseodymium ions. In *LASER 2006*, pages 233–241. Springer, 2007.

[33] DJ Larson, JC Bergquist, JJ Bollinger, Wayne M Itano, and DJ Wineland. Sympathetic cooling of trapped ions: A laser-cooled two-species nonneutral ion plasma. *Physical Review Letters*, 57(1):70, 1986.

[34] D.R. Lide. *CRC Handbook of Chemistry and Physics, 85th Edition*. CRC Handbook of Chemistry and Physics, 85th Ed. Taylor & Francis, 2004.

[35] WW Macalpine and RO Schildknecht. Coaxial resonators with helical inner conductor. *Proceedings of the IRE*, 47(12):2099–2105, 1959.

[36] Martin John Madsen. Advanced ion trap development and ultrafast laser-ion interactions. 2006.

[37] Reina Maruyama. *Optical trapping of ytterbium atoms*. PhD thesis, University of Washington, 2003.

[38] James J McLoughlin, Altaf H Nizamani, James D Siverns, Robin C Sterling, Marcus D Hughes, Bjoern Lekitsch, Björn Stein, Seb Weidt, and Winfried K Hensinger. Ytterbium ion trap experiment towards scalable quantum technology. *arXiv preprint arXiv:1007.4010*, 2010.

[39] DM Meekhof, C Monroe, BE King, WM Itano, and DJ Wineland. Generation of nonclassical motional states of a trapped atom. *Physical Review Letters*, 76(11):1796, 1996.

[40] J Migdalek. Influence of core polarisation on relativistic oscillator strengths for lowest sp transitions in Yb II-Hf IV spectra. *Journal of Physics B: Atomic and Molecular Physics*, 13(6):L169, 1980.

[41] Kristian Mølhave. *Construction of and experiments with a linear Paul trap*. Institut for Fysik og Astronomi, Århus Universitet, 2000.

[42] Klaus Mølmer and Anders Sørensen. Multiparticle entanglement of hot trapped ions. *Physical Review Letters*, 82(9):1835, 1999.

[43] Marc R. Momme. Aufbau eines Lasersystems zum Photo-Ionisieren von Ytterbium, 2013.

[44] Thomas Monz, Philipp Schindler, Julio T Barreiro, Michael Chwalla, Daniel Nigg, William A Coish, Maximilian Harlander, Wolfgang Hänsel, Markus Hennrich, and Rainer Blatt. 14-qubit entanglement: Creation and coherence. *Physical Review Letters*, 106(13):130506, 2011.

[45] W Neuhauser, M Hohenstatt, PE Toschek, and H Dehmelt. Localized visible Ba$^+$ mono-ion oscillator. *Physical Review A*, 22(3):1137, 1980.

[46] W Neuhauser, M Hohenstatt, PE Toschek, and HG Dehmelt. Visual observation and optical cooling of electrodynamically contained ions. *Applied Physics*, 17(2):123–129, 1978.

[47] M.A. Nielsen and I.L. Chuang. *Quantum computation and quantum information*. Cambridge University Press, 2010.

[48] Jeremy L O'Brien. Optical quantum computing. *Science*, 318(5856):1567–1570, 2007.

[49] S Ohtsubo, M Fujioka, H Higaki, K Ito, H Okamoto, H Sugimoto, and SM Lund. Experimental study of coherent betatron resonances with a Paul trap. *Physical Review Special Topics-Accelerators and Beams*, 13(4):044201, 2010.

[50] S. Olmschenk, KC Younge, DL Moehring, DN Matsukevich, P. Maunz, and C. Monroe. Manipulation and detection of a trapped Yb^+ hyperfine qubit. *Physical Review-Section A-Atomic Molecular and Optical Physics*, 76(5):52314–52314, 2007.

[51] W. Paul. Electromagnetic traps for charged and neutral particles. 1990.

[52] JD Prestage, Go J Dick, and L Maleki. New ion trap for frequency standard applications. *Journal of Applied Physics*, 66(3):1013–1017, 1989.

[53] L. Ricci, M. Weidemüller, T. Esslinger, A. Hemmerich, C. Zimmermann, V. Vuletic, W. König, and T.W. Hänsch. A compact grating-stabilized diode laser system for atomic physics. *Optics Communications*, 117(5-6):541–549, 1995.

[54] M Roberts, P Taylor, SV Gateva-Kostova, RBM Clarke, WRC Rowley, and P Gill. Measurement of the $^2S_{1/2}$–$^2D_{5/2}$ clock transition in a single $^{171}Yb^+$ ion. *Physical Review A*, 60(4):2867, 1999.

[55] Nils Roth. Konzeption und Bau eine Wellenlängenmessgerätes, 2012.

[56] Th Sauter, R Blatt, W Neuhauser, and PE Toschek. Quantum jumps observed in the fluorescence of a single ion. *Optics Communications*, 60(5):287–292, 1986.

[57] H Schaaf, U Schmeling, and G Werth. Trapped ion density distribution in the presence of He-buffer gas. *Applied Physics*, 25(3):249–251, 1981.

[58] JD Siverns, LR Simkins, S Weidt, and WK Hensinger. On the application of radio frequency voltages to ion traps via helical resonators. *Applied Physics B*, 107(4):921–934, 2012.

[59] Anders Sørensen and Klaus Mølmer. Quantum computation with ions in thermal motion. *arXiv preprint quant-ph/9810039*, 1998.

[60] Dan Stick, WK Hensinger, Steven Olmschenk, MJ Madsen, Keith Schwab, and Chris Monroe. Ion trap in a semiconductor chip. *Nature Physics*, 2(1):36–39, 2005.

[61] EW Streed, TJ Weinhold, and David Kielpinski. Frequency stabilization of an ultraviolet laser to ions in a discharge. *Applied Physics Letters*, 93(7):071103–071103, 2008.

[62] O. Svelto. *Principles of Lasers*. Springer Verlag, 2009.

[63] F v. Busch and W Paul. Über nichtlineare Resonanzen im elektrischen Massenfilter als Folge von Feldfehlern. *Zeitschrift für Physik*, 164(5):588–594, 1961.

[64] Andreas Wallraff, David I Schuster, Alexandre Blais, L Frunzio, R-S Huang, J Majer, S Kumar, Steven M Girvin, and Robert J Schoelkopf. Strong coupling of a single photon to a superconducting qubit using circuit quantum electrodynamics. *Nature*, 431(7005):162–167, 2004.

[65] Phillip Wieburg. Ein hochstabiler optischer Resonator zur Frequenzstabilisierung eines Diodenlasers im ultravioletten Spektralbereich, 2012.

[66] D. J. Wineland, R. E. Drullinger, and F. L. Walls. Radiation-pressure cooling of bound resonant absorbers. *Phys. Rev. Lett.*, 40:1639–1642, Jun 1978.

[67] DJ Wineland, Wayne M Itano, JC Bergquist, and Randall G Hulet. Laser-cooling limits and single-ion spectroscopy. *Physical Review A*, 36(5):2220, 1987.

[68] N. Yu and L. Maleki. Lifetime measurements of the $4f^{14}5d$ metastable states in single ytterbium ions. *Physical Review A*, 61(2):022507, 2000.

[69] Jascha Zander. Aufbau eines Lasersystems zur Külung von Ytterbium(+)-Ionen, 2013.

[70] Christoph Zipkes. *A Trapped Single Ion Inside a Bose-Einstein Condensate*. PhD thesis, University of Cambridge, 2011.

Eidesstattliche Erklärung

Hiermit bestätige ich, dass die vorliegende Arbeit von mir selbstständig verfasst wurde und ich keine anderen als die angegebenen Hilfsmittel - insbesondere keine im Quellenverzeichnis nicht benannten Internet-Quellen - benutzt habe und die Arbeit von mir vorher nicht einem anderen Prüfungsverfahren eingereicht wurde. Die eingereichte schriftliche Fassung entspricht der auf dem elektronischen Speichermedium.
Ich bin damit einverstanden, dass die Masterarbeit veröffentlicht wird.

Hamburg, den 30.04.2014

Phillip Wieburg